THE ASTROPHYSICAL JOURNAL, 316:323–348, 1987 May 1

RADIATIVE BOW SHOCK MODELS OF HERBIG-HARO OBJECTS[1]

PATRICK HARTIGAN
Department of Planetary Sciences, University of Arizona

AND

JOHN RAYMOND AND LEE HARTMANN
Harvard-Smithsonian Center for Astrophysics
Received 1986 July 17; accepted 1986 October 15

ABSTRACT

We have constructed bow shock models of HH objects from a collection of 43 radiative planar shock models. The bow shock models are used to predict the line ratios and line profiles expected from HH objects, and comparison of the model with four different regions containing HH objects indicates that a single unifying model—a radiating bow shock formed around a "bullet" of dense gas plowing into the ambient medium—can account for the bulk of the existing observations. Spectral line profiles expected from stationary cloudlets and moving bullets are discussed for a variety of shock velocities, orientation angles, and emission lines. We show that for particular bow shock orientations double-peaked profiles are predicted in spatially unresolved spectra, and that such models provide a natural explanation for the spectra of HH 32 and the HH objects in Cepheus A. In general, analysis of many bright HH objects is consistent with the interstellar bullet model, although one object in particular is better fitted with a shocked cloudlet model. We present a simple analytic formula that can be used to estimate the shock velocity and bow shock orientation from a single high-resolution observation of a low-excitation line.

Subject headings: line formation — line profiles — radiative transfer — shock waves — stars: pre–main-sequence

I. INTRODUCTION

Herbig-Haro (HH) objects are semistellar emission-line sources usually located near bipolar flows from pre–main-sequence stars. The large proper motions (Luyten 1971; Cudworth and Herbig 1979; Herbig and Jones 1981) and radial velocities (Schwartz and Dopita 1980) of HH objects imply supersonic motions, and the general accepted model for the radiation from these objects is that the emission lines occur as gas cools behind a shock (see Schwartz 1983 for a review). Several authors (e.g., Dopita 1978; Raymond 1979) have modeled the observed emission-line ratios from HH objects using plane-parallel shocks. These attempts have only been partially successful in reproducing the observed UV and visible line strengths. The major problem is the presence of bright lines of highly ionized species like C IV in addition to prominent low-excitation lines like S II and O I. The result is that no single plane-parallel model fits the observed data. Some HH objects exhibit extraordinary line profiles. Line widths in HH objects can approach 500 km s^{-1} for a single knot (see Hartigan *et al.* 1986). How can such line widths be present in an object of at most a few Earth masses that is only 1500 AU in diameter? Line profiles of HH objects in Cepheus A and HH 32 are double-peaked for the low excitation lines of H, N II, and S II. This structure can not be explained satisfactorily by any plane-parallel model (Hartigan, Mundt, and Stocke, 1986).

One possible resolution to these puzzles would be to have the emission from HH objects arise from the cooling region behind a bow shock (Schwartz 1978). The bow shock could form either around a dense clump of gas ejected into the ambient cloud (as in the "bullet" model; Norman and Silk 1979 and Tenorio-Tagle and Rózyczka 1984), or from a supersonic stellar wind impinging upon a clump of gas in the flow (as in the "shocked cloudlet" model; Schwartz 1978). The bow shock geometry produces a mixture of shock velocities because only the component of motion perpendicular to the bow is slowed, and this perpendicular kinetic energy converted into line emission. Such a senario could explain the failure of plane-parallel models to predict the observed line ratios from HH objects. In addition, a bow shock will splatter material away from the central obstacle, producing large line widths from a small volume. The double-peaked line profiles might arise from viewing the bow shock from oblique angles.

Previous work on bow shocks indicates that this line of reasoning could be quite fruitful. Hartmann and Raymond (1984) found that a model based on approximating the oblique shock regions of the bow shock by a series of plane-parallel shock models was able to produce large line widths, as well as line ratios that agreed better with the observations than planar shock models. Several authors (Choe, Böhm, and Solf 1985; Raga and Böhm 1985; Raga 1986) have constructed position-velocity diagrams from bow shocks and have found fairly good agreement with observations.

In this work we present more refined bow shock models than those of Hartmann and Raymond (1984). The present models are constructed from a set of 43 planar shock models which sample a wide range of shock velocities (20 km $s^{-1} \leq V_s \leq$ 400 km s^{-1}). We also explore a variety of bow shapes, preshock densities, and preshock ionization conditions. The bow shock model is discussed in § II, and the planar shock models are presented in § III. In § IV the bow shock models are used to predict the emission-line ratios expected for various shock velocities, and also to predict the emission-line profiles

[1] Observations obtained at the Multiple Mirror Telescope Observatory (MMTO) operated jointly by the University of Arizona and the Smithsonian Institution.

when the bow shock is viewed from an arbitrary angle. Both the shock velocity and bow orientation can be estimated from a simple analytic formula we present in § IV. The predictions are then applied to individual regions containing HH objects in § V, where we compare the model predictions with new and existing high-resolution spectra of HH objects. Although the bow shock models were constructed with the intent to model HH objects, they might also be useful in other astrophysical contexts (such as galactic jets).

II. THE BOW SHOCK MODEL

a) Geometry and Kinematics

Figure 1 depicts the geometry of a bowshock. One must know the postshock velocity V_2 and angle θ of the emitting gas to model bow shock line profiles. In the frame of reference of the bow shock, the preshock material is incident from the left at the shock velocity V_s and enters the bowshock at an angle ξ from vertical. This angle is determined once a bow shape $Z(R)$ is chosen. All models assume axial symmetry. The observer views the bow shock at an angle ϕ from the bow's apex. To calculate the line emission the bow shock is divided into 200 annuli of constant ξ. The emission from each annulus is taken to be that from a plane-parallel shock of velocity $V_\perp$ (the planar models are discussed in § III) weighted by the area of the annulus. Co-addition of the annuli over the entire bow gives the expected emission-line profiles and ratios from the object. The parallel component $V_\parallel$ of the incident velocity is continuous across the shock, and immediately behind the shock the perpendicular velocity $V_\perp$ diminishes according to the shock jump conditions (by a factor of 4 for a strong shock). The hot ($\gtrsim 10^5$ K for shock velocities of interest) gas must cool to about 10^4 K before optical line radiation becomes visible. The gas becomes denser as it cools, and since ρv is conserved the velocity must decrease. A complete analysis would require solving the two-dimensional hydrodynamic flow problem inside the volume bounded by the bow shock with radiative cooling included. This problem has been solved, but only with simplified radiative cooling rates, and without the detailed photoionization and time-dependent ionization calculations needed to compute accurate line intensities and profiles (Sandford and Whitaker 1983; Rózyczka and Tenorio-Tagle 1985*a*, *b*). Therefore we use existing numerical calculations of the bow shock shape to make the following approximate models for the emission lines.

We assume the cooling distance to be small compared with the size of the bow shock, so that the radiation originates in a narrow shell next to the bow (see § III for a discussion of this point). Guided by the planar shock models, we choose a fixed temperature for the line of interest (typically 10^4 K for optical lines) and calculate the expected postshock $V_\perp$ taking into account both the jump conditions at the shock interface (velocity decrease by a factor of 4 for a strong shock) and the effect of cooling (decrease by an additional factor of about 10). Taking $V_\parallel$ to be unchanged during cooling allows the velocity V_2 and deflection angle θ to be calculated. Hence, the line profile consists of the co-addition of a series of expanding rings of emitting material (Fig. 1). The final line profile is calculated by smoothing the points with a Gaussian whose width arises from thermal motions of the emitting ion plus any instrumental broadening.

b) Line Profiles

We begin construction of theoretical line profiles by calculating a probability distribution for the radial velocity of a particle on an expanding ring of material. The probability distribution must then be weighted by the area of the ring and the line intensity as obtained from the planar shock models.

From Figure 1, the radial velocity of a particle on the ring at azimuthal angle ψ is given by

$$V_r = V_2(\cos\theta\cos\phi + \sin\theta\sin\phi\cos\psi)\,. \tag{1}$$

Emission from HH objects is optically thin except perhaps for the resonance lines Lyα, C II λ1335, and C IV λ1550. Thus, for an axially symmetric ring, the probability distribution of radial velocity is proportional to $(\partial\psi/\partial V_r)_{\theta,\phi,V_2}$, so the probability of a given radial velocity $P(V_r)$ is given by

$$P(V_r) = \frac{1}{\pi}\,[w_2{}^2 - (V_r - w_1)^2]^{-1/2}\,, \tag{2}$$

where $w_1 = V_2\cos\theta\cos\phi$, and $w_2 = V_2\sin\theta\sin\phi$. The probability distribution is double-peaked (Fig. 2), with the two peaks corresponding to the extreme radial velocities on the

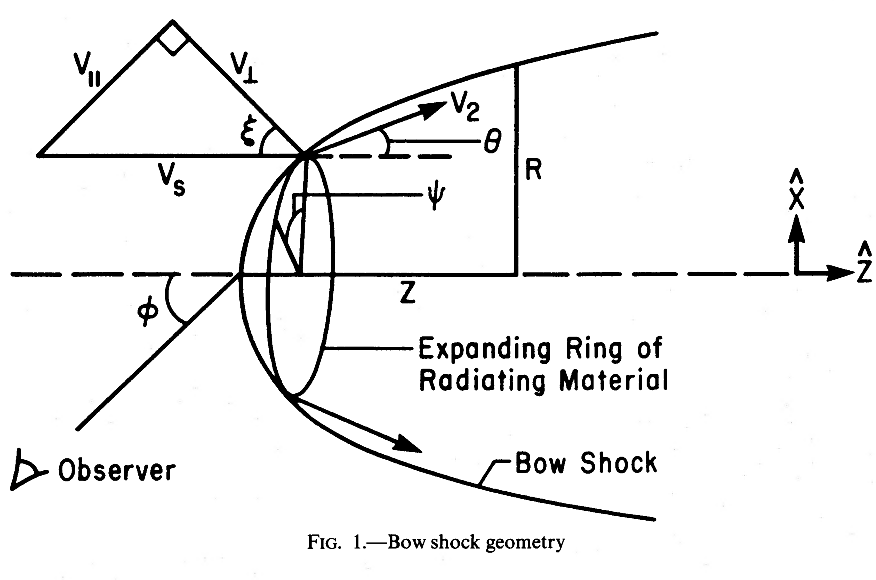

FIG. 1.—Bow shock geometry

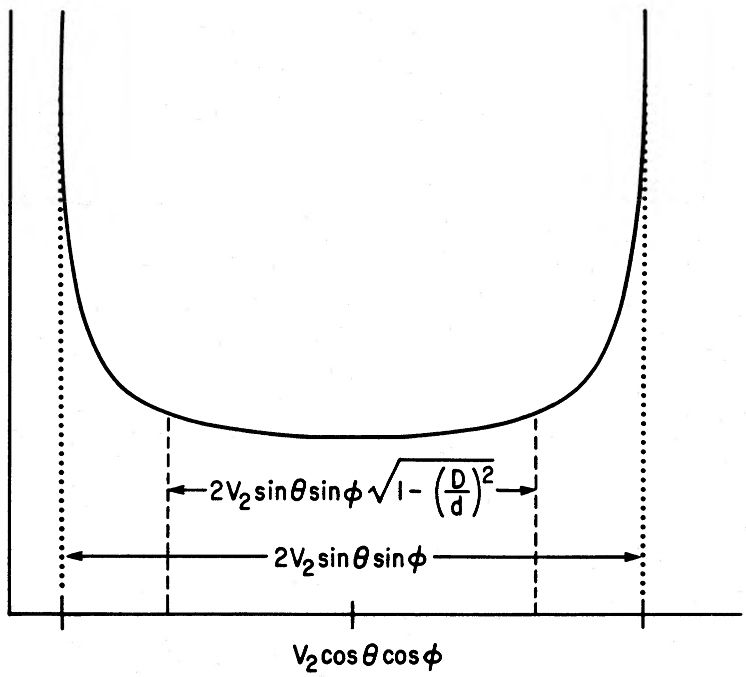

FIG. 2.—Probability distribution of radial velocities observed from the expanding ring of material in Fig. 1. The radial velocities between the dashed lines are excluded when the spectrograph slit is narrower than the emitting ring. The parameters d and D are the ring and slit diameters, respectively.

ring. The probability distribution (2) assumes the entire expanding ring to be included in the observing aperture. Since spectroscopic observations are usually obtained through a slit, we would like to know how the distribution alters when a slit is positioned along the z-axis. The effect of such a slit will be to exclude emission fron azimuthal angles between ψ_c and $\pi - \psi_c$, and also between $-\psi_c$ and $-\pi + \psi_c$, where $\psi_c = \sin^{-1}(D/d)$, D is the diameter of the slit projected on the sky, and d is the diameter of the emission ring. Thus, there is a set of radial velocities of width $2V_2 \sin\theta \sin\phi[1 - (D/d)^2]^{1/2}$ centered at $V_2 \cos\theta \cos\phi$ which is no longer seen (Fig. 2). As the slit narrows, the excluded region widens until only the extreme radial velocities are seen (at the front and back of the ring).

The probability formalism easily accounts for the effects of a finite slit, and we have included this capability in our models. However, since spectrographic slit widths are typically 1″.5, seeing 1″–2″, and telescope tracking errors $\sim$1″, the observed line profiles probably include emission over areas 2″–3″ at least. Since this is on the order of the sizes of many HH objects, the line profiles reported in this work typically include the entire emission from the bow shock.

c) *Bow Shock Shape*

The bow shape $Z(R)$ is one of the input parameters to the bow shock models. We have investigated the shape proposed by DeYoung and Axford (1967) (hereafter the DA shape) as well as a class of shapes similar to that proposed by Raga (1986). Raga used an inverse method assuming postshock ionization equilibrium to determine the bow shape near the apex produced by a spherical obstacle. Normalizing the coordinates R and Z by the obstacle radius R_0 ($z = [Z/R_0]$, $r = [R/R_0]$) we can write the Raga shape as

$$z(r) = \frac{0.42r^2 + 0.136r^4}{1 + 0.273(M^2 - 1)^{-1/2} r^3} . \qquad (3)$$

Some difficulties are encountered with the shape at large R and Z, since it does not approach the Mach angle, and the incident angle ξ decreases, instead of increasing uniformly as one proceeds from the apex. Since the shape (3) never reaches the Mach angle ($V_\perp = Cs$ = sound speed), the bow shock never terminates.

If we disregard the denominator term, we retain Raga's paraxial solution and achieve a shape that reaches the Mach angle at some (r, z) where line emission must cease. We have used this modified Raga shape ($z = 0.42r^2 + 0.136r^4$) to model bow shock line emission. Since the obstacle may not be spherical, we would like to be able to investigate general shapes of the form $z = Ar^2 + Br^4$. To this end we parameterize a class of bow shapes according to

$$z(r) = \alpha r^2 + \alpha^3 \beta r^4 , \quad \alpha \text{ and } \beta \text{ constants} . \qquad (4)$$

With this parameterization β has a clearly defined physical significance. The quadratic and quartic terms in equation (4) are of equal magnitude when $r = \alpha^{-1}\beta^{-1/2}$. At this value of r the incident angle ξ_c is given by $\tan \xi_c = (dz/dr)_{r=\alpha^{-1}\beta^{-1/2}}$, so that

$$\xi_c = \tan^{-1}(6\beta^{-1/2}) . \qquad (5)$$

This critical angle represents the point where the quadratic shape gives way to the steeper quartic shape. Incident angles exceeding ξ_c lie on the quartic curve and have less relative importance to the final emission line profile.

Suppose we were to normalize the shape $Z(R)$ by $\bar{R}_0 = kR_0$, where k is a constant. Then with $z = Z/R_0 = z/k$ and $r = R/R_0 = r/k$ we find $\bar{z}(\bar{r}) = (k\alpha)\bar{r}^2 + (k\alpha)^3 \beta \bar{r}^4$ so that $\bar{\alpha} = k\alpha$ and $\bar{\beta} = \beta$. Hence, although β is independent of the normalization, the value of α depends upon the choice of the normalization constant R_0. Any two shapes with the same value of β are therefore the same for modeling purposes. For example, the shapes $z_1 = 0.5r_1^2 + 0.1r_1^4$ and $z_2 = r_2^2 + 0.8r_2^4$ produce identical line profiles for each emission line and identical line ratios. The parameter α has a physical significance only if a physical significance is attached to R_0. For instance, if R_0 is always chosen to be the radius of a spherical obstacle, then the bow shock flairs away from the obstacle more for smaller values of α. In the models, R_0 is chosen to make the angular diameter of the radiating bow shock a few arcseconds, consistent with the observed sizes of HH objects. Once a value of R_0 is chosen, the absolute flux of Hβ as seen from Earth can be calculated and compared with observed values.

Różyczka and Tenorio-Tagle (1985*a*, *b*) have computed the shapes of bow shocks using a two-dimensional numerical hydrodynamics code. They find that radiative cooling makes the shape of a 200 km s^{-1} bow shock much narrower than either the 100 or 400 km s^{-1} bow shocks, greatly reducing the importance of the bow shock wings. They also find that if one begins with a spherical obstacle, the cloud shock flattens the obstacle and produces a progressively more blunt bow shock. Evolution into a more flattened shape requires several hundred years for typical cloud parameters, and on that time scale the cloud is likely to be disrupted by Rayleigh-Taylor instabilities (Różyczka and Tenorio-Tagle 1985*b*). While transit times inferred from proper motions of HH object knots from the exciting stars to their present positions are hundreds of years, some knots are observed to turn on and fade away with lifetimes of a few decades (Herbig and Jones 1981). If we interpret this to mean that these knots move out in a low-density flow of similar velocity until they reach the high-density ambient medium at the end of the cavity cleared by the outflow, then the observed lifetimes of a few decades are appropriate, and we do not expect significant flattening or disruption of the clouds. However, such short lifetimes cast some doubt on the correctness of the assumption of a steady state bow shock shape.

Not all shapes can be represented accurately by a quartic polynomial, however. The DA shape is given by

$$z(r) = -2 \ln \left[\cos \left(\frac{r}{2} \right) \right] , \quad (6)$$

where $R_0 = h$ is the scale height for normalization. Expanding equation (6) in powers of r near $r = 0$ we find $\alpha = 0.25$, $\beta = 0.667$, and $\xi_c = 82^\circ\!.3$. Since ξ_c is larger for DA than for Raga (where $\xi_c = 77^\circ\!.3$), we might expect DA to emphasize low velocity shocks away from the apex more than the Raga shape. The opposite is in fact true—DA is more blunt-shaped than Raga, giving rise to larger fluxes in the high-excitation lines like O III and C IV as compared to Hβ. The problem is that the DA shape cannot be approximated by a quartic polynomial far from the apex ($r \approx \pi$). The shape $z(r) = 0.42r^2 + 1.0r^4$ (hereafter shape A) reproduces the observed line profiles fairly well and is used extensively in the bow shock models. Shape A has a critical angle of $58^\circ\!.5$, so the higher shock velocities near the apex are relatively more important to the final line profile for this shape than for the Raga shape. As for the other shapes, the numerical integration terminates when shape A reaches the Mach angle.

d) *The Obstacle*

For simplicity we neglect absorption of far-side bow shock emission by dust in the obstacle. We can estimate the amount of absorption likely to be present as follows. Schwartz (1978) showed that for $\gamma = 5/3$, the pressure P_0 in the obstacle is related to the incident ram pressure by $P_0 = 0.88\eta_w V_s^2$. This relation imposes a constraint on the number density (η_0) and temperature (T_0) in the obstacle in terms of the preshock number density (η_w) and the shock velocity (V_s) of the wind. We find

$$\eta_0 T_0 = 2.1 \times 10^8 \left(\frac{\eta_w}{100 \text{ cm}^{-3}} \right) \left(\frac{V_s}{200 \text{ km s}^{-1}} \right)^2 \text{ cm}^{-3} \text{ K} . \quad (7)$$

The number density in the obstacle must exceed that of the shocked wind, so we take $\eta_0 > 3 \times 10^4$ cm^{-3} (Brugel, Böhm, and Mannery 1981). The temperature of the obstacle exceeds the ambient cloud's temperature, about 30 K. Using equation (7), we find $\eta_0 < 7 \times 10^6$ cm^{-3} and $T_0 < 7 \times 10^3$ K. Adopting $\eta_0 = 10^5$ cm^{-3}, and 1500 AU for the obstacle diameter yields an obstacle mass of 160 $M_\oplus$, and a maximum hydrogen column density for the obstacle of 2.2×10^{21} cm^{-2}. Using Spitzer's (1978) relation between N_H and $E_{B-V} = 0.38$, so that $A_v = 1.1$ along the center of the obstacle, suggesting that the obstacle could have some influence on the line profiles, especially in the UV. Seab and Shull (1983) showed that about 50% of silicate grains and up to 85% of graphite grains can be expected to survive a 100 km s^{-1} shock. Hence, extinction due to postshock grains could in principle affect the line profiles, although the column density of this material should be about 10 times less than the maximum column density through the obstacle.

We also ignore the shock propagating into the cloudlet in our calculations. Following Schwartz (1978), for $V_w = 200$ km s^{-1}, $\eta_0 = 10^5$ cm^{-3} and $\eta_w = 100$ cm^{-3} we find 6 km s^{-1} for this "cloudlet shock" velocity. This is a very weak shock and should not affect the line profiles significantly, except perhaps for the neutral lines. The shock will take about 600 yr to traverse the obstacle, on the order of the sound crossing time for $T_0 = 10^3$ K.

III. PLANAR SHOCK MODELS

a) *Input Parameters*

The planar shock models used in this work are described in detail by Raymond (1979) and Cox and Raymond (1985). A grid of shock models closely spaced in velocity is needed to accurately model bow shock emission since the effective shock velocity $V_\perp$ varies markedly across the bow. Our planar models were typically computed every 20 km s^{-1} to follow the variation of line fluxes with shock velocity.

The ionization state of the preshock gas greatly influences the line fluxes and ratios expected from a shock (see Cox and Raymond 1985). Unfortunately, the preshock ionization conditions in front of a bow shock are not easily determined. Some very hard UV radiation escapes near the apex where $V_\perp$ is large, and if this radiation succeeds in fully ionizing all the incident material, then we should employ a set of fully preionized (H^+, He^{++}) planar models in the bow shock calculations. On the other hand, the situation could resemble "equilibrium" preionization, where the ionized state of the preshock gas is the same as that in front of a planar shock of velocity $V_\perp$. With such a scenario, the preshock ionization can vary from fully ionized at the apex to neutral near the edges of the bow. To investigate these two cases we initially compiled a set of fully preionized (H^+, He^{++}) shock models and a set of equilibrium preionization shock models with preshock number density 100 cm^{-3}. When it became clear (see § IV*b*) that equilibrium preionization models fit the data somewhat better than the

1987ApJ...316..323H

fully preionized case, we compiled another set of equilibrium preionized models with higher preshock density (1000 cm^{-3}) to determine the importance of collisional deexcitation for the emission lines.

An approximate calculation of the ionization state of gas entering a 200 km s^{-1} bow shock shows the gas to be 50%–70% neutral for $V_{\perp} = 40$–160 km s^{-1}, and a significant ionized fraction persists even for very small effective shock velocities in the bow shock wings. Based on the methods described by Cox and Raymond (1985), we find that this more realistic preshock ionization state implies a 15% increase in the absolute Hβ flux, little change in the [O III]/Hβ ratio, and a 50% increase in [O II]/Hβ. The strength of the two photon continuum is roughly doubled.

We fixed the logarithmic abundance ratios H:He:C:N:O:Ne:Mg:Si:S:Ar:Ca:Fe:Ni at the following "cosmic" values, 12.0:10.93:8.52:7.96:8.82:8.12:7.52:7.62:7.20:6.90:6.30:7.50:6.30 for all planar models except A100, a 100 km s^{-1} model with abundances of Fe and Si reduced by $10^{1/2}$ to give an indication of the effects of depletion of refractory elements due to dust condensation. This depletion is similar to what occurs after sputtering and grain-grain collisions in the post-shock flow have destroyed most of the grains (Seab and Shull 1983), although the actual depletion factor depends on the shock velocity since higher velocity shocks destroy grains more effectively than low-velocity shocks. The preshock magnetic field was taken to be negligible (0.1 μG) in all models except B100, where $B = 10$ μG. The preshock temperature was fixed at 10^4 K for all models. A radiative transfer parameter R_{max} (Cox 1972) was taken to be 1, a value more appropriate for the nonplanar geometry of a bowshock than the planar value of 3. For cases where the cooling distance approaches R_0, an even smaller value of R_{max} might be appropriate. Differences between fluxes reported here and those of Cox and Raymond (1985) are principally due to this parameter. Calculation of emission-line fluxes was terminated when the gas temperature reached 10^3 K.

Planar shock models require an input radiation field in order to calculate the ionization state of the preshock gas for each element. This input radiation field was taken to be the output radiation field from a planar shock of similar velocity. Although the shock code predicts the preshock ionization state of H and He, for the equilibrium models we chose to fix these values using the results of Shull and McKee (1979), who performed a somewhat more detailed analysis of the preshock ionization problem. It is especially important to choose the correct value for the incident fraction of He^+, since He II λ304 is an important coolant. Step sizes in the program were carefully chosen to adequately sample the temperatures near 10^4 K where the cooling gas becomes optically thick to Lyman-continuum radiation. Undersampling of this region can lead to as much as a factor of 2 smaller fluxes for the bright optical forbidden lines. Due to the absence of molecular cooling in the models, the 20 km s^{-1} results could be somewhat inaccurate. Without molecular cooling it is difficult to predict the low-excitation infrared emission-line fluxes accurately—the fluxes from these lines are probably overestimated in the models. Numerical difficulties plague the shock models for $V_s > 300$ km s^{-1}, and these model fluxes are more uncertain than the fluxes predicted for low-velocity shocks, especially for the neutral lines (O I, N I, and C I). Moreover, shocks faster than 200 km s^{-1} are thermally unstable (McCray, Stein, and Kafatos 1975; Innes, Giddings, and Falle 1986). Effects of this instability on the average emission-line spectrum are not yet understood, but an additional turbulent contribution to the line widths is likely. Comparison of various theoretical shock models with similar preshock conditions and elemental abundances at the Workshop on Nebulae (Péquinot 1986) indicated a typical scatter in predicted line ratios of 30% for the strong lines, though the model codes occasionally disagree by as much as a factor of 3.

Several complications must be kept in mind when comparing model shocks with observations. Resonance line photons are scattered within the emitting gas and in the intervening interstellar gas when the gas is optically thick (as can occur for resonant lines of abundant ions). This severely attenuates the C II λ1335 and C IV λ1550 lines in the spectra of supernova remnants (Raymond *et al.* 1981). The large line widths and cylindrical symmetry of HH objects will reduce the importance of resonance line scattering within the emitting region, but the interstellar C II absorption line is strong enough to affect the observed intensity of the λ1335 line significantly. Intensities of the He II λ1640, 4686 lines depend on the radiative transfer of He II Lyman photons, which is not treated in detail. We assume case B for recombination, which occurs primarily at low temperatures and velocities, and case A for excitation, which occurs in the high-temperature region just behind the shock. These assumptions introduce about a factor of 2 uncertainty in the predicted line intensities. The present model also ignores excitation from the metastable $1s2s\ ^3S$ level of He I, so the intensity of the λ10830 line is underestimated (Raymond 1979).

b) Planar Shock Results

Since the shock velocity was the only parameter varied within a given set of planar shock models, our results clarify how the shock velocity, preshock density, and preshock ionization state individually influence the emission line fluxes. Results of the equilibrium preionization models with $\eta = 100$ cm^{-3} (E models), and the equilibrium preionization with $\eta = 1000$ cm^{-3} (D models) appear in Table 1. The fully preionized (I models) are shown in Table 2. Equilibrium models reach complete preionization for shock velocities >180 km s^{-1}. There are significant differences between equilibrium and fully preionized models at lower shock velocities, however, especially for the O I and O II lines. Increasing the preshock density in the equilibrium models makes all lines brighter (the Hβ flux scales linearly with η), but by differing amounts depending upon the importance of collisional deexcitation for a given line. The [O II] λ3727/Hβ ratio, for example, decreases dramatically due to collisional quenching when η is increased from 100 cm^{-3} to 1000 cm^{-3}. Ratios of the permitted UV lines to Hβ are quite insensitive to η.

For $V_s > 60$ km s^{-1} the optical forbidden lines tend to increase monotonically in strength relative to Hβ with increasing shock velocity until the postshock density becomes large enough to collisionally deexcite the lines. The UV lines are typically invisible until V_s becomes large enough to create the ion of interest, and then suddenly become prominant. As V_s increases the UV lines slowly decrease in intensity relative to Hβ. These trends reflect the increasing amount of ionizing photons produced at the higher postshock temperatures as V_s increases. Recombining hydrogen at 10^4 K absorbs these photons, and the energy is radiated away in the Balmer lines (lowering the UV/Hβ ratio for a given UV line) and optical forbidden lines (increasing the ratios of [O I]/Hβ, [N II]/Hβ, etc.). This behavior apparently continues at very high shock

TABLE 1

PREDICTED ENERGY FLUXES FROM PLANAR SHOCKS WITH EQUILIBRIUM PREIONIZATION

MODEL	E400	E350	E300	E280	E260 D260	E240	E220 D220	E200	E180 D180	E160	E140 D140	E130	E120 D120	E110	E100 D100	E90	E80 D80	E60 D60	E40 D40	E30 D30	E20 D20	A100[1]	B100[2]
V_s (km/s)	400	350	300	280	260	240	220	200	180	160	140	130	120	110	100	90	80	60	40	30	20	100	100
X(H I)	0	0	0	0	0	0	0	0	0	0	0	0	0	0	0.31	0.62	0.92	0.99	1	1	1	0.31	0.31
Y_o (He I)	0	0	0	0	0	0	0	0	0	0	0	0	0	0	0.66	0.95	1	1	1	1	1	0.66	0.66
Y_1 (He II)	0	0	0	0	0	0	0	0	0.30	0.60	0.75	0.80	0.88	0.93	0.34	0.05	0	0	0	0	0	0.34	0.34
N_o (cm^{-3})	100	100	100	100	100	100	100	100	100	100	100	100	100	100	100	100	100	100	100	100	100	100	100
					1000		1000		1000		1000		1000		1000		1000	1000	1000	1000	1000		
d_{c3} (AU)	7720	4630	2230	1720	1250	839	549	323	120	55	29	25	26	27	17	10	5.1	11	59	258	2540	26	61
					126		57		14		3.5		3.9		2.8		0.7	1.5	10	34	357		
d_{c4} (AU)	7720	4630	2230	1710	1250	826	532	308	107	44	16	11	10	10	8.0	4.4	1.0	1.2	6.4	34	608	8.8	9.4
					125		53		11		1.6		1.0		0.8		0.1	0.1	0.7	3.3	61		
τ_{c3} (yr)	564	421	437	329	334	469	567	493	411	281	297	248	268	260	149	90	41	83	334	991	5760	290	162
					46		123		106		38		48		29		5.9	12	68	141	936		
τ_{c4} (yr)	545	374	221	181	142	103	73	49	23	13	8.0	6.8	6.8	7.0	7.1	5.9	1.9	2.3	10.6	43	566	8.0	7.9
					14		7.4		2.3		0.8		0.7		0.8		0.3	0.2	1.2	4.2	57		
$F_{H\beta}$[5]	26.5	23.1	17.9	15.5	13.7	11.8	10.0	8.32	6.99	5.59	3.93	3.52	3.01	2.58	3.55	3.44	2.73	1.05	0.22	6.7-2	9.4-3	3.59	3.29
					136		99.6		69.6		39.2		30.0		35.3		27.6	10.7	2.32	0.73	9.8-2		
He II 304	1440	1420	1280	1260	1210	1150	1120	1080	1850	3450	6520	6940	6640	5680	816	13	1	0	0	0	0	856	1010
					1230		1130		1870		6550		6680		825		0.9	0	0	0	0		
C III 977	387	402	463	501	539	586	653	730	757	764	1740	1870	1900	1960	957	154	4.8	1.3	0.8	0.1	0	1020	1050
					577		694		804		1780		1930		969		3.6	0.5	0.1	0.1	0		
N III 991	72	74	85	92	98	105	116	129	128	202	241	180	159	156	81	5.4	0.1	0	0	0	0	87	89
					102		120		132		246		161		83		0.1	0	0	0	0		
O VI 1035[3]	4140	3990	6320	6750	6780	7000	7010	6940	4510	656	11	1.1	0	0	0	0	0	0	0	0	0	0	0
					6820		7020		4550		11		0		0		0	0	0	0	0		
Ne V] 1141[3]	86	88	101	110	118	131	149	156	93	46	6.9	1.9	0.5	0.1	0	0	0	0	0	0	0	0	0
					119		149		94		7.0		0.5		0		0	0	0	0	0		
S III 1198	80	84	97	104	111	119	132	146	152	178	240	207	193	188	115	41	2.8	1.3	1.7	0.8	0	125	121
					115		135		157		246		198		118		2.2	0.6	0.5	0.7	0		
Si III 1206	81	87	103	111	120	129	144	161	173	187	183	158	205	299	340	129	2.8	0.4	0	0	0	117	358
					128		154		184		196		210		351		2.8	0.4	0	0	0		
Ly α 1216	4970	4640	4130	4010	3940	3870	3840	3840	3840	3840	3860	3840	3850	3860	5200	5540	6430	7150	9750	13500	24800	5230	5060
					4340		4090		4030		4020		3990		5420		6430	7080	9730	12700	24800		
O V] 1218	305	305	347	379	406	451	510	608	738	523	106	38	13	4.0	0	0	0	0	0	0	0	0	0
					408		512		742		107		13		0		0	0	0	0	0		
N V 1240[3]	293	297	365	392	420	473	532	606	550	718	145	45	15	4.4	0	0	0	0	0	0	0	0	0
					425		535		553		147		15		0		0	0	0	0	0		
C II 1336	97	106	124	132	144	153	173	195	214	223	343	404	433	464	303	167	15	11	18	35	93	339	317
					132		159		200		342		463		323		17	12	19	31	93		

NOTE.—All fluxes are normalized to Hβ = 100. The parameters X, Y_0, and Y_1, refer to the ionization state of the preshock gas, N_0 is the preshock density; d_{c3} and d_{c4} are the distances between the shock and the position where $T = 10^3$ and 10^4 K, respectively; and τ_{c3} and τ_{c4} are the corresponding cooling times.

[1] Abundance of Fe and Si depleted by $\sqrt{}10$.

[2] $B = 10\ \mu$G.

[3] Line is a doublet.

[4] The ^4P–^2P intersystem transitions consist of five closely spaced lines (Mendoza 1983). There are seven lines of O IV] and Si IV] between 1393 Å and 1407 Å.

[5] 10^{-4} ergs cm^{-2} s^{-1} through front of shock.

TABLE 1—*Continued*

MODEL	E400	E350	E300	E280	E260 D260	E240	E220 D220	E200	E180 D180	E160	E140 D140	E130	E120 D120	E110	E100 D100	E90	E80 D80	E60 D60	E40 D40	E30 D30	E20 D20	A100	B100
Si IV 1397[3]	33	34	40	43	46	50	56	62	61	65	70	84	142	214	149	7.6	0.1	0	0	0	0	51	163
					48		57		63		72		139		152		0.1	0	0	0	0		
O IV] 1402[4]	220	222	245	264	277	298	325	361	438	487	294	195	147	108	0.5	0	0	0	0	0	0	5.0	6.2
					280		326		441		297		151		4.7		0	0	0	0	0		
N IV] 1486	38	38	41	44	46	50	54	60	56	111	99	64	50	40	3.5	0	0	0	0	0	0	3.7	4.4
					47		54		57		100		51		3.5		0	0	0	0	0		
C IV 1549[3]	533	547	618	670	706	758	830	978	1040	1250	2600	2090	1580	1150	79	1.3	0	0	0	0	0	79	93
					719		840		1050		2620		1620		76		0	0	0	0	0		
[Ne V] 1574	7	7.2	8.2	8.9	9.5	11	12	13	7.6	3.9	0.7	0.2	0.1	0	0	0	0	0	0	0	0	0	0
					9.6		12		7.7		0.7		0.1		0		0	0	0	0	0		
[Ne IV] 1601	27	27	29	31	32	34	38	41	37	35	25	19	14	8.6	0.3	0	0	0	0	0	0	0.2	0.3
					40		45		44		30		17		0.3		0	0	0	0	0		
He II 1640	109	107	82	76	68	60	55	50	58	81	116	106	89	67	5.8	0	0	0	0	0	0	9.7	7.3
					69		56		71		117		89		9.4		0	0	0	0	0		
O III] 1663[3]	130	130	145	156	164	175	190	209	243	286	268	212	197	202	105	3.2	0	0	0	0	0	112	115
					167		194		247		274		201		107		0.1	0	0	0	0		
N III] 1750[4]	35	35	39	41	43	46	50	55	55	80	99	81	76	76	43	3.8	0.1	0	0	0	0	46	45
					46		53		58		102		77		44		0.1	0	0	0	0		
Si III] 1891	89	92	106	115	122	131	143	157	166	182	189	170	203	271	282	151	4.2	0.5	0.1	0.1	0	97	288
					133		155		181		207		216		295		4.3	0.5	0.1	0.1	0		
C III] 1908	194	191	210	226	238	256	279	304	314	320	603	682	719	753	420	128	10	3.3	3.5	0.8	0	450	445
					268		311		350		640		740		429		8.1	1.5	0.6	0.8	0		
N II] 2141[3]	11	11	11	12	12	12	13	14	15	18	22	21	21	21	14	14	2.2	1.6	2.5	3.4	0.2	15	14
					13		15		16		24		22		15		2.4	1.5	2.1	3.3	0.2		
C II] 2326[4]	252	267	240	228	219	211	213	217	221	222	289	336	364	378	240	168	34	30	68	156	599	265	237
					283		256		255		320		413		265		40	34	72	145	637		
Si II] 2340[4]	29	32	22	19	15	13	12	11	10	9.1	8.3	9.9	9.8	9.8	7.6	6.7	4.9	4.4	9.4	20	76	2.7	7.0
					27		19		15		12		15		9.1		5.5	4.6	9.6	19	84		
[Ne IV] 2423[3]	111	115	130	142	150	162	179	197	186	175	136	108	84	56	2.1	0.1	0	0	0	0	0	1.5	1.9
					114		144		156		117		73		1.3		0	0	0	0	0		
[O II] 2470	60	61	60	60	60	60	62	63	66	68	69	63	61	60	41	40	7.7	2.3	0.8	0.5	0.4	45	36
					83		88		99		110		104		73		15	4.7	1.5	0.7	0.4		
Mg II 2799[3]	1060	1200	853	696	553	441	360	291	247	198	143	150	138	122	69	65	32	32	56	191	2490	81	55
					1080		707		499		335		298		102		64	69	113	214	2370		
Mg I 2852	83	119	156	128	119	91	74	60	51	46	38	42	36	26	2.9	2.6	1.7	1.7	5.4	17	106	5.8	2.6
					136		95		62		58		58		7.2		2.8	3.0	5.9	10	223		
[O II] 3726	77	105	128	138	150	163	184	210	247	291	330	336	355	378	271	290	85	44	25	18	12	302	271
					27		36		54		90		108		100		31	26	28	20	14		
[O II] 3729	27	38	48	53	58	65	75	89	110	138	166	172	188	210	165	186	48	33	31	25	18	184	177
					9.2		12		19		32		39		39		12	11	18	20	20		
[Ne III] 3869	101	104	84	75	69	64	64	66	68	72	75	69	73	79	50	14	1.0	0.3	0.2	0.3	0	49	48
					81		71		72		81		78		49		0.6	0.1	0.1	0.3	0		
Ca II 3945[3]	356	494	565	485	442	359	298	243	204	169	123	134	114	84	17	16	12	12	25	59	679	26	13
					654		471		325		237		221		35		19	17	33	64	802		
[Ne III] 3968	32	33	27	24	22	20	20	21	22	23	24	22	23	25	16	4.4	0.3	0.1	0.1	0.1	0	16	15
					26		23		23		26		25		16		0.2	0	0	0.1	0		
[S II] 4072[3]	196	260	277	236	216	179	154	131	114	99	83	85	76	64	25	20	7.1	6.3	9.4	26	103	31	19
					350		263		196		171		169		55		19	21	29	35	128		
Ca I 4227	10	16	38	30	36	30	26	22	18	17	16	18	17	15	2.9	1.4	1.1	1.3	2.5	4.1	25	5.1	4.4
					37		31		21		20		22		6.3		1.8	2.0	4.0	4.7	36		

TABLE 1—*Continued*

MODEL	E400	E350	E300	E280	E260 D260	E240	E220 D220	E200	E180 D180	E160	E140 D140	E130	E120 D120	E110	E100 D100	E90	E80 D80	E60 D60	E40 D40	E30 D30	E20 D20	A100	B100
[O III] 4363	22	21	23	25	25	27	29	32	36	43	42	34	33	34	18	0.6	0	0	0	0	0	19	19
					28		31		38		43		34		18		0	0	0	0	0		
[Fe III] 4658	5.7	5.7	6.2	6.5	6.8	7.1	7.7	8.4	8.9	9.2	9.7	9.7	11	13	10	9.4	2.3	0.5	0.2	0.1	0.1	3.4	9.5
					8.1		9.0		10		11		13		11		2.5	0.1	0	0.2	0.1		
Hβ 4861	100	100	100	100	100	100	100	100	100	100	100	100	100	100	100	100	100	100	100	100	100	100	100
					100		100		100		100		100		100		100	100	100	100	100		
[O III] 4959	90	86	90	96	98	104	110	117	130	152	160	142	139	143	75	2.4	0	0	0	0	0	79	80
					90		104		127		159		139		75		0.1	0	0	0	0		
[O III] 5007	263	249	260	278	284	301	318	340	378	443	466	413	406	417	219	7.0	0.2	0	0	0	0	228	233
					262		302		368		463		405		219		0.2	0	0	0	0		
[N I] 5200[3]	10	26	76	55	68	51	41	32	25	26	31	39	38	34	6.4	4.4	3.8	8.8	45	134	614	11	6.9
					17		14		6.9		9.1		14		3.1		1.0	3.4	34	112	719		
[N II] 5755	8.7	8.0	6.7	6.4	6.1	5.8	5.6	5.5	5.4	5.7	6.2	5.9	5.8	5.8	3.7	3.8	1.0	0.8	1.3	1.6	0	4.1	3.5
					10		9.4		8.8		9.2		8.5		5.0		1.4	0.9	1.1	1.6	0		
He I 5876	22	27	31	27	26	25	22	19	16	17	23	25	25	24	10	3.7	1.1	0.5	0	0	0	11	11
					25		22		17		22		24		9.8		1.0	0.4	0	0	0		
[O I] 6300	446	631	765	609	583	455	372	293	234	208	193	211	188	152	28	16	19	44	134	304	1100	46	21
					736		517		321		290		292		58		26	54	155	313	1340		
[O I] 6363	149	210	255	203	194	152	124	98	78	69	64	70	63	51	9.3	5.2	6.2	15	45	101	368	15	7.1
					245		172		107		97		97		19		8.8	18	52	104	448		
[N II] 6548	82	93	87	85	82	80	77	74	73	72	66	66	63	61	32	31	16	17	22	23	1.9	36	33
					32		35		39		47		49		26		13	15	18	25	2.2		
Hα 6563	299	295	291	290	291	291	291	293	294	296	297	297	298	300	283	289	310	320	388	456	615	282	284
					293		292		295		295		297		281		307	327	383	444	613		
[N II] 6583	243	275	255	251	243	235	228	219	215	211	193	193	188	179	95	91	48	50	65	69	5.5	105	96
					96		103		115		138		145		76		39	44	55	74	6.4		
[S II] 6716	18	39	114	85	107	87	77	64	54	56	66	78	78	74	24	19	8.2	17	62	209	851	34	28
					27		25		14		18		26		8.4		2.6	7.9	56	171	1020		
[S II] 6731	41	89	224	174	203	166	146	124	108	110	121	139	137	125	42	32	14	23	53	151	587	57	42
					62		55		32		41		57		19		6.0	17	85	172	737		
[Ar III] 7136	16	15	14	14	14	14	15	15	16	18	21	21	22	22	14	4.5	1.3	0.6	0.5	0.2	0	14	14
					15		15		17		22		23		15		0.6	0.4	0.1	0.2	0		
[Ca II] 7307[3]	65	97	135	116	113	94	80	65	54	47	39	43	38	30	5.2	3.9	3.0	3.8	8.0	17	132	8.5	4.4
					149		116		77		63		62		12		5.1	5.3	11	20	167		
[O II] 7320	45	45	44	45	45	45	46	47	49	51	51	47	45	45	31	30	5.7	1.7	0.7	0.4	0.3	34	27
					61		65		73		82		77		54		11	3.5	1.1	0.5	0.3		
[O II] 7331	36	36	36	36	36	36	37	38	39	41	41	38	37	36	25	24	4.6	1.4	0.5	0.3	0.2	27	22
					49		52		59		66		62		43		8.9	2.8	0.9	0.4	0.2		
[Fe II] 8617	57	48	47	40	34	27	22	18	15	13	10	12	10	7.7	2.4	2.1	2.4	3.5	8.6	19	71	1.0	2.0
					51		34		23		19		18		3.8		3.1	4.1	9.5	19	84		
[C I] 8727	63	93	105	83	75	56	44	33	26	24	22	17	15	12	3.3	2.8	2.0	1.7	2.7	3.1	2.1	4.7	1.9
					119		81		51		50		33		8.5		4.7	3.8	5.2	6.2	14.2		
[S III] 9069	51	59	51	43	36	29	23	17	14	15	18	19	18	16	6.5	4.6	5.7	6.9	16	11	0.2	6.9	6.9
					43		28		16		22		8.0		7.3		5.0	3.4	5.4	11	0		
[S III] 9532	132	153	133	111	95	75	60	45	36	39	48	49	47	42	17	12	15	18	41	28	0.4	18	18
					111		72		42		58		21		19		13	8.9	14	28	0		
[C I] 9823	56	139	400	300	358	290	249	193	146	144	166	110	107	95	28	19	18	21	34	35	19	40	18
					123		126		75		91		58		21		11	22	64	86	156		
[C I] 9850	165	412	1190	890	1060	860	740	571	432	426	494	328	317	281	83	58	47	62	102	104	57	119	52
					364		374		221		269		171		63		33	64	189	254	464		

TABLE 1—*Continued*

MODEL	E400	E350	E300	E280	E260 D260	E240	E220 D220	E200	E180 D180	E160	E140 D140	E130	E120 D120	E110	E100 D100	E90	E80 D80	E60 D60	E40 D40	E30 D30	E20 D20	A100	B100
[S II] 10289	68	91	97	83	76	63	54	46	40	35	29	30	27	23	8.8	6.8	2.5	2.2	3.3	9.1	36	11	6.6
+10339					121		91		68		60		59		19		6.5	7.5	10	12	45		
[S II] 10323	63	83	89	75	69	57	49	42	36	32	26	27	24	21	8.0	6.2	2.3	2.0	3.0	8.3	33	10	6.0
+10373					112		84		63		55		54		18		5.9	6.8	9.2	11	41		
[NI] 10402[3]	32	45	42	35	29	22	18	14	12	9.9	8.3	8.8	7.6	5.8	1.7	1.5	0.9	0.9	1.8	4.2	20	2.3	1.1
					52		33		21		19		18		4.0		1.9	2.3	5.2	6.7	25		
He I 10830	32	39	43	37	36	32	29	24	19	21	28	31	31	30	26	29	3.8	2.1	1.1	0.6	0.2	26	26
					36		30		21		28		32		26		3.8	2.1	1.1	0.6	0.2		
[Ne II] 12.8μ	129	195	345	287	314	301	281	228	173	167	198	190	183	166	47	27	27	48	128	228	23	55	47
					278		291		175		193		190		53		25	41	116	263	3.1		
[Ne III] 15.6μ	169	237	274	214	195	149	111	77	53	50	58	61	61	60	31	12	2.5	1.4	1.3	1.7	0	29	32
					113		72		32		36		40		20		1.0	0.3	0.7	1.7	0		
[Fe II] 26.0μ	292	519	815	691	679	566	506	425	363	339	340	375	351	301	90	63	59	104	280	618	2080	41	83
					419		325		206		244		317		76		45	95	310	650	2680		
[Si II] 35.3μ	11	27	48	42	41	34	32	30	28	31	37	337	372	376	153	88	43	151	993	2800	10300	114	158
					9.0		6.4		4.9		6.9		149		57		8.2	33	502	1790	12700		
[O I] 63.2μ	18	45	211	148	219	241	308	283	223	182	216	188	191	182	66	35	22	53	180	447	2770	116	39
					59		330		247		94		131		50		10	34	215	501	3870		
2 photon	1960	1770	1480	1420	1370	1340	1330	1320	1320	1320	1340	1340	1340	1350	1580	1720	2170	2600	4010	6070	12450	1600	1550
					1590		1460		1420		1410		1400		1620		2170	2580	3920	5660	12450		

TABLE 2

PREDICTED ENERGY FLUX FROM PLANAR SHOCKS

MODEL	I 180	I 160	I 140	I 120	I 100	I 80	I 60	I 40	I 20
V_s (km/s)	180	160	140	120	100	80	60	40	20
N (cm^{-3})	100	100	100	100	100	100	100	100	100
d_{c3} (AU)	154	92	63	46	36	32	38	161	16
d_{c4} (AU)	142	80	54	35	26	24	26	31	-
τ_{c3} (yr)	354	337	202	202	177	149	119	188	397
τ_{c4} (yr)	27	18	16	13	12	14	17	22	-
$F_{H\beta}$ [1]	6.98	5.72	4.75	3.16	2.18	1.54	1.07	0.66	0.31
He II 304	929	803	710	646	512	412	394	395	364
C III 977	777	785	860	2420	3840	2600	497	1.1	0
N III 991	133	148	242	312	305	214	29	0.1	0
O VI 1035	5350	1980	239	68	0	0	0	0	0
Ne V] 1141	108	69	31	6.0	0.2	0	0	0	0
S III 1198	155	159	206	269	279	290	159	3.5	0
Si III 1206	174	184	194	215	390	996	543	65	0.1
Ly α 1216	3830	3830	3780	3850	3940	4080	4190	3980	3270
O V] 1218	743	711	396	108	6.0	0	0	0	0
NV 1240	570	697	590	149	7.0	0	0	0	0
C II 1336	214	224	229	367	593	691	759	196	0.7
Si IV 1397	63	66	76	165	321	230	11	0.2	0
O IV] 1402	427	512	500	411	181	13	0	0	0
N IV] 1486	59	76	139	141	72	9.3	0	0	0
C IV 1549	1080	1290	1820	3590	2210	180	0.6	0	0
[Ne V] 1574	8.8	5.7	2.7	0.6	0	0	0	0	0
[Ne IV] 1601	40	37	36	31	14	0.6	0	0	0
He II 1640	43	40	39	45	51	53	54	54	51
O III] 1663	236	281	290	327	334	262	33	0.8	0
N III] 1750	57	62	93	118	119	100	24	0.1	0
Si III] 1891	168	178	186	210	307	721	537	143	2.1
C III] 1908	319	325	334	707	1170	1000	370	3.5	0
N II] 2141	15	16	19	24	26	30	40	17	0.3
C II] 2326	220	220	214	296	432	494	560	310	17
Si II] 2340	9.7	8.8	8.5	8.2	9.5	16	18	13	1.7
[Ne IV] 2423	194	185	182	169	84	3.9	0	0	0
[O II] 2470	65	68	65	69	68	71	88	40	2.9
Mg II 2799	234	187	127	100	100	127	165	517	79
Mg I 2852	49	41	31	16	4.2	5.1	6.1	9.3	12
[O II] 3726	242	286	314	379	438	552	791	527	114
[O II] 3729	108	135	159	209	268	392	690	504	123
[Ne III] 3869	69	71	72	85	99	98	25	5	0.1
Ca II 3945	196	160	110	58	23	28	32	33	51
[Ne III] 3968	22	22	23	27	31	31	7.9	1.6	0
[S II] 4072	111	94	76	58	40	38	36	30	8.3
Ca I 4227	18	16	14	11	4.6	2.6	2.8	2.6	3.6
[O III] 4363	35	42	43	49	51	42	6.3	0.2	0
[Fe III] 4658	8.9	9.2	9.0	11	16	20	23	20	3.9
Hβ 4861	100	100	100	100	100	100	100	100	100
[O III] 4959	127	147	153	178	188	167	32	1.8	0.1
[O III] 5007	370	428	445	518	546	487	92	5.1	0.4
[N I] 5200	24	21	19	17	9.6	9.0	14	23	23
[N II] 5755	5.4	5.3	5.5	6.3	6.7	7.4	9.5	5.6	0.4
He I 5876	14	13	12	13	14	15	15	16	17
[O I] 6300	226	184	142	98	43	29	32	31	18
[O I] 6363	75	61	47	33	14	9.6	11	10	6.0
[N II] 6548	71	69	65	59	54	59	69	58	14
Hα 6563	294	296	296	299	305	309	311	311	304
[N II] 6583	211	203	190	175	160	173	204	172	40
[S II] 6716	53	50	48	48	39	45	65	89	49
[S II] 6731	106	99	93	87	67	70	88	100	45
[Ar III] 7136	16	17	18	22	25	27	26	1.6	0.1
[Ca II] 7307	53	44	34	21	7.4	7.1	7.8	7.8	12
[O II] 7320	48	50	48	51	50	53	65	30	2.2
[O II] 7331	39	40	38	41	41	42	53	24	1.8
[Fe II] 8617	15	12	8.9	5.4	3.3	4.1	4.7	4.7	2.7
[C I] 8727	25	21	14	8.4	3.9	4.3	5.2	5.0	3.3
[S III] 9069	13	12	10	12	12	12	11	3.3	0.5
[S III] 9532	34	30	27	30	30	31	28	8.7	1.4
[C I] 9823	144	122	79	61	33	30	42	45	36
[C I] 9850	426	361	235	180	98	88	123	135	108

TABLE 2—*Continued*

MODEL	I 180	I 160	I 140	I 120	I 100	I 80	I 60	I 40	I 20
[S II] 10289 +10339	39	33	27	20	14	13	13	11	2.9
[S II] 10323 +10373	35	30	24	19	13	12	11	9.7	2.7
[N I] 10402	11	8.9	6.4	4.3	2.5	2.7	2.8	2.6	1.1
He I 10830	18	16	15	16	16	17	16	17	18
[Ne II] 12.8μ	166	132	100	90	75	64	64	50	27
[Ne III] 15.6μ	53	45	42	48	55	56	18	6.9	0.7
[Fe II] 26.0μ	351	313	263	205	140	128	131	141	135
[Si II] 35.3μ	28	28	227	276	282	245	171	238	346
[O I] 63.2μ	214	193	126	133	117	86	63	63	55
2 photon	1320	1320	1300	1340	1390	1470	1530	1420	1100

NOTE.—The incident material is fully ionized (H^+, He^{++}). All variables are defined as for Table 1.

[1] Hβ flux in units of 10^{-4} ergs cm^{-2} s^{-1} out of the front of the shock.

velocities (1000 km s^{-1}; Binette, Dopita, and Touhy 1985). We include predictions for a large number of bright emission lines in the extreme UV and far-IR which may become observable in the near future with space-borne instruments.

c) Cooling Distances

Our bow shock models assume that the cooling distance is small compared with the size of the emitting bow shock (typically 1500 AU). We can use the plane-parallel models to determine the cooling distance as a function of shock velocity and preshock density (Table 1). The equilibrium preionization results are fitted well by a power law when $V_s > 60$ km s^{-1}. We find

$$d_{c3} = 12\left(\frac{V_s}{100\ \mathrm{km\ s^{-1}}}\right)^{4.67}\left(\frac{100\ \mathrm{cm^{-3}}}{\eta}\right)\ \mathrm{AU}\,, \tag{8}$$

where d_{c3} is the distance between the planar shock and the point where $T = 10^3$ K, η is the preshock number density of neutrals plus ions, and V_s is the shock velocity. For $\eta = 300$ cm^{-3}, the cooling distance exceeds 1500 AU for $V_s > 350$ km s^{-1}. Hence, the assumption of small cooling distances is valid unless V_s is large and η small. Even for large V_s the assumption of small cooling distances will be valid over most of the bow shock since $V_\perp \approx V_s$ only near the apex of the bow.

IV. BOW SHOCK RESULTS

a) Estimating the Shock Velocity and Orientation Angle of an Arbitrary Radiating Bow Shock from a Single Observation

The shock velocity V_s and orientation angle ϕ are two of the most important physical parameters in any bow shock model. For a stationary cloudlet or for a bullet colliding with a stationary medium, the shock velocity represents the speed of the outflowing material. Knowledge of the shock velocity enables one to estimate the stellar mass outflow rate as well as predict emission-line fluxes and ratios from a bow shock. Together, the orientation angle and shock velocity determine the flow's age and enable one to predict line profiles and proper motions for the HH object. In what follows we show that for a wide range of bow shocks both V_s and ϕ can be estimated from a single high-resolution spectrum.

Assume that the cooling distance is small compared with the size of the bow shock (see § III), so that the emission arises from a thin surface of revolution about the z-axis. Let us calculate the full width of an emission line (FWZI) as seen by an observer at angle ϕ. For a given emitting ring (Fig. 1), the radial velocity reaches a maximum at the top of the ring, and a minimum at the bottom. Hence, to find the extreme radial velocities of the bow shock emission it is sufficient to search along the curve defined by the intersection of the bow and the xz plane.

Since the perpendicular component of the incident velocity diminishes by a factor of ~ 40 by the time the gas radiates (see § II*a*), this velocity is negligible compared with V_s, and we take it to be zero, so that $V_2 = V_\parallel$, and $\theta = (\pi/2) - \xi$. The radial velocity of the emitting gas in the xz plane is then (cf. eq. [1])

$$V_r = V_s \sin\zeta(\sin\xi\cos\phi \pm \cos\xi\sin\phi)\,, \tag{9}$$

where the + and − signs refer to the top and bottom halves of the curve, respectively. Next set $\partial V_r/\partial\xi = 0$ to obtain the extreme maximum radial velocity along the top half of the bow. This occurs when $\xi = (\pi/2) - (\phi/2)$, and substituting this value into equation (9) we find the maximum radial velocity $MX = (V_s/2)[1 + \cos\phi]$. The maximum radial velocity will be reached for all viewing angles ϕ provided ξ ranges from 0 to $\pi/2$, i.e., the line profile of interest radiates over the entire bow shock. The highest excitation lines (e.g., C IV) violate this condition since they exist only near the apex where $V_\perp$ is large. A similar calculation for the minimum radial velocity MN can be performed on the bottom half of the bow, and this extreme radial velocity occurs when $\xi = \phi/2$, so that $MN = -(V_s/2)[1 - \cos\phi]$.

Since the formulae for MX and MN were derived in the frame of reference of the bow shock, the observed maximum and minimum radial velocities will shift by the radial velocity γ of the bow shock with respect to the exciting star. For a stationary cloudlet $\gamma = 0$, whereas for a bullet plowing into a stationary medium $\gamma = -V_s\cos\phi$. The observed maximum and minimum radial velocities from a bow shock become

$$MX = \frac{V_s}{2}(1 + \cos\phi) + \gamma$$

and

$$MN = -\frac{V_s}{2}(1 - \cos\phi) + \gamma\,. \tag{10}$$

The full width of an emission line is just

$$\mathrm{FWZI} = MX - MN = V_s\,. \tag{11}$$

Equations (10) and (11) are remarkably simple, and the results are *independent* of the most uncertain aspects of bow shock modeling, such as preshock density, bow shock shape, the ionization state and temperature of the incident gas, the elemental abundances, reddening, etc. Hence, the shock velocity can be estimated from a single high-resolution line profile of any low-excitation line (e.g., Hα). If one invokes either the bullet or cloudlet models, and the velocity of the exciting source with respect to the observer is known (for example from CS, NH_3 or CO line observations), then the maximum or minimum radial velocity observed gives the orientation angle of the outflow. However, such estimates of ϕ are not always precise, since MX and MN determine the cosine of ϕ (eq. [10]), so that ϕ can be measured accurately when $\phi \approx 90°$ (flows approximately in the plane of the sky), but all oblique flows ($0° < \phi < 45°$, $135° < \phi < 180°$) have values of MX or MN near zero radial velocity.

Using equation (10), the centroid radial velocity (average between MX and MN) is

$$V_c = \frac{MX + MN}{2} = \frac{V_s}{2} \cos \phi + \gamma \,, \qquad (12)$$

so that this velocity is *not* the radial velocity γ of the HH object, as has been widely assumed in the past. V_c and γ differ since the radiating gas moves with respect to the obstacle causing the bow shock. The relations (10) and (11) are extremely useful diagnostics and provide a starting point for any line profile analysis. Including instrumental and thermal broadening, and nonzero $V_\perp$ in the numerical models discussed in the next section alters the analytical results only slightly.

b) *Theoretical Line Profiles*

The line profiles discussed in this section were generated using the bow shock model in § II. Figure 3 presents a series of theoretical line profiles. Figures 3*a*–3*g* display the effect of varying orientation angles while keeping the other variables fixed. The Hα line profile is symmetrical about zero velocity when the HH object moves in the plane of the sky $\phi \approx 90°$; Fig. (3*a*), but as ϕ decreases the profile becomes increasingly asymmetric, with two distinct peaks appearing for viewing angles less than 45°. When $\phi = 0$ the two peaks arise from different areas on the bow shock; the high radial velocity component arises from near the bow apex, and the low radial velocity from the wings (for the bullet model). When $\phi = 45°$ the distinction between peaks is no longer as clear, since the expansion of postshock material distributes emission over a range of radial velocities (Figs. 1 and 2). The line width at $\phi = 90°$ arises solely from this expansion.

Axial symmetry of the bow shock models not only dictates the symmetry about zero radial velocity for all lines when $\phi = 0$ but also ensures a relationship between profiles observed at angle ϕ and those observed at $180 - \phi$. The radial velocities of each expanding ring of material simply change sign when viewed at $180 - \phi$ (Fig. 1). Hence, the line profiles from $180 - \phi$ are reflections about zero of the profiles viewed at angle ϕ (Figs. 3*g* and 3*h*).

As the previous section predicts, the FWZI of the Hα emission line remains constant as ϕ varies. This width exceeds the shock velocity slightly for each spectrum in Figure 3. The maximum radial velocity is somewhat larger and the minimum radial velocity somewhat more negative in the model than the analytic predictions (eqs. [10] and [11]) due to the instrumental and thermal broadening present in the models. The bow shock models show that relations (10) and (11) can still be used to estimate V_s and ϕ provided the values of MX and MN are measured as follows. Let the FWHM of the smoothing Gaussian be SM. This width contains both instrumental and thermal broadening terms. Let $MX0.1$ and $MN0.1$ represent the observed maximum and minimum radial velocities at 0.1 of the peak intensity. Set

$$MX = MX0.1 - SM/2$$

and

$$MN = MN0.1 + SM/2 \,. \qquad (13)$$

Equations (10), (11), and (13) are used in § V as the starting points for the analysis of individual regions containing HH objects. Although estimates of V_s obtained in this manner are quite accurate, estimates of ϕ can be uncertain when the angle is small. From equation (10), the difference between MX and MN for $\phi = 0°$ and $\phi = 30°$ is only 0.067 V_s, so that any small shift of the line profile (which might be caused by a bullet plowing into a moving, instead of fixed, medium, for example) can influence the estimated ϕ markedly.

Figures 3*i*–3*p* present 100 km s^{-1} and 400 km s^{-1} line profiles identical in every other respect with the 200 km s^{-1} models in Figures 3*a*–3*h*. As with the previous models, the line widths slightly exceed the shock velocity for all orientation angles, and equations (10), (11), and (13) successfully predict V_s and ϕ for each profile. When plotted logarithmically, the Hα flux increases more rapidly at lower shock velocities (Table 1). This behavior causes the apex emission to become relatively more important at lower bow shock velocities. The 100 km s^{-1} profiles exhibit only a single peak at oblique ϕ since the high radial velocity apex emission has increased and merged with the low radial velocity emission. In general, double-peak Hα profiles occur only when $V_s > 150$ km s^{-1} km s^{-1} and $\phi < 45°$.

Figures 3*q* and 3*r* illustrate the effect of bow shape on the line profile. The high radial velocity emission is more pronounced for the DA shape (Fig. 3*q*) than for shape A (Fig. 3*e*). The Raga shape (Fig. 3*r*) has the weakest high radial velocity component. These trends follow from the remarks regarding shape in § II*c*.

For a stationary cloudlet, the centroid of the radiating gas will be blueshifted when $\phi > 90°$ (eq. [12]), so the orientation angle of the cloudlet in Figure 3*s* is taken to be 150° to facilitate comparison with the bullet model in Figure 3*e* ($\phi = 30°$). The two profiles have identical velocity centroids and widths (eqs. [10] and [12]), but the cloudlet profile is the mirror image of the bullet profile. In general, line profiles from a stationary cloudlet with orientation angle ϕ will mirror those produced by a bullet with orientation angle $180 - \phi$. This follows from the axial symmetry of the problem. From Figure 2, the emission from a single emitting ring of material from a bullet with orientation angle $180 - \phi$ is symmetrical, and it is centered at radial velocity $W = -V_2 \cos \theta \cos \phi$. If the bullet is viewed at an angle ϕ, the emission shifts to $V_2 \cos \theta \cos \phi$, and coverting to cloudlet geometry we obtain $U = V_2 \cos \theta \cos \phi + V_s \cos \phi$ as the center. Hence, the average of U and W is simply V_c (cf. eq. [12]), the centroid velocity, so that the emission from a single emitting ring of material is reflected about V_c. Since the line profile consists of the co-addition of many such rings, it too is reflected about V_c when one changes from bullet to cloudlet geometry.

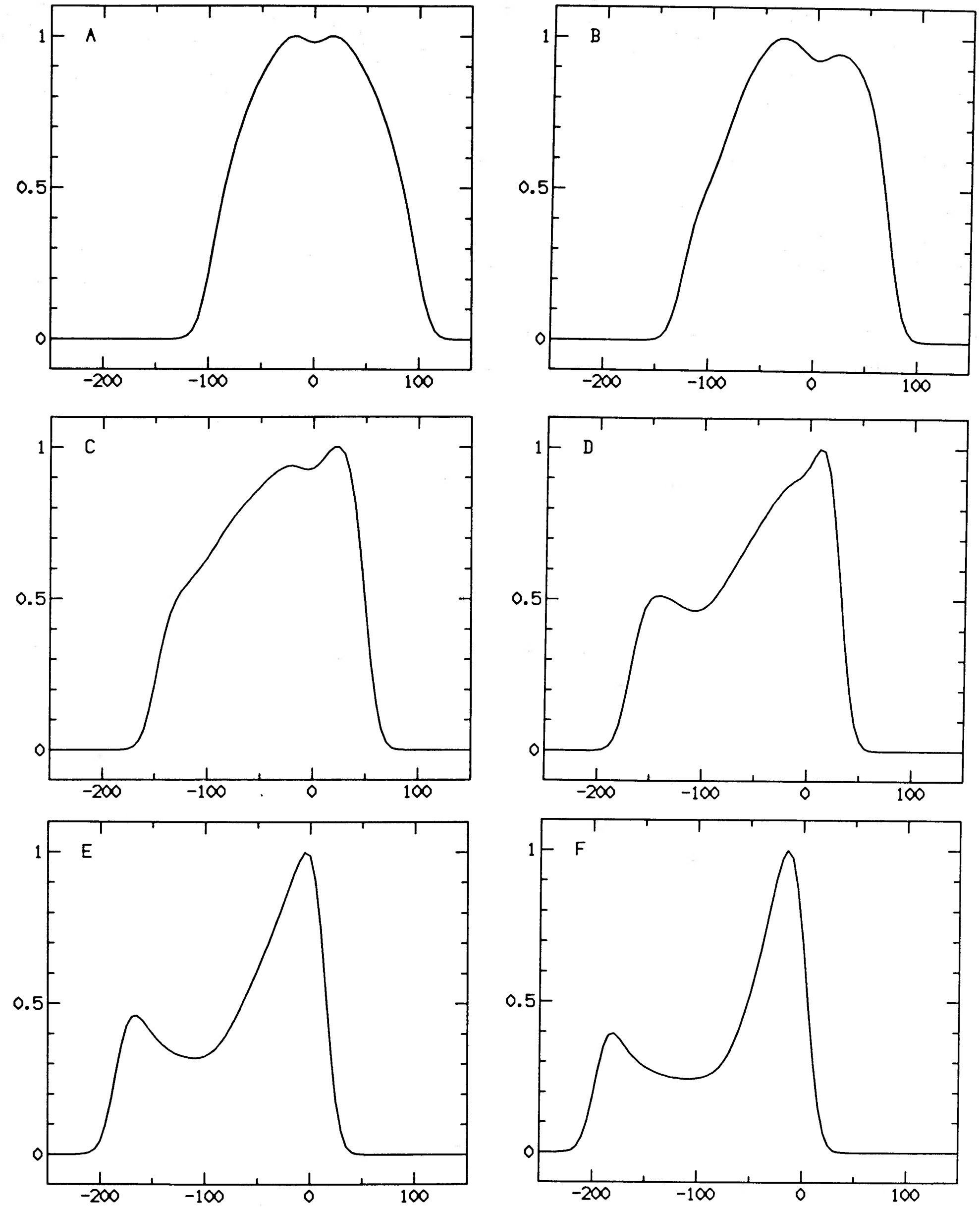

FIG. 3.—Theoretical line profiles from the bow shock models. Radial velocities in km s^{-1} with respect to the exciting source are plotted vs. relative fluxes (normalized to unity at the peak). (*a*) Shows Hα from a 200 km s^{-1} shock with equilibrium preionization, bullet geometry, orientation angle (cf. Fig. 1) $\phi = 90°$, bow shock shape A, slit wider than the HH object, $T = 10^4$ K, preshock density 300 cm^{-3}, and instrumental broadening 12 km s^{-1} FWHM. The remaining profiles have the following variations: (*b*) $\phi = 75°$. (*c*) $\phi = 60°$. (*d*) $\phi = 45°$. (*e*) $\phi = 30°$. (*f*) $\phi = 15°$. (*g*) $\phi = 0°$. (*h*) $\phi = 180°$. (*i*) $V_s = 100$ km s^{-1}, $\phi = 90°$. (*j*) $V_s = 100$ km s^{-1}, $\phi = 60°$. (*k*) $V_s = 100$ km s^{-1}, $\phi = 30°$. (*l*) $V_s = 100$ km s^{-1}, $\phi = 0°$. (*m*) $V_s = 400$ km s^{-1}, $\phi = 90°$. (*n*) $V_s = 400$ km s^{-1}, $\phi = 60°$. (*o*) $V_s = 400$ km s^{-1}, $\phi = 30°$. (*p*) $V_s = 400$ km s^{-1}, $\phi = 0°$. (*q*) $\phi = 30°$, DA shape. (*r*) $\phi = 30°$, Raga shape. (*s*) $\phi = 150°$, cloudlet geometry. (*t*) $\phi = 30°$, slit/HH = 0.4. (*u*) $\phi = 30°$, fully preionized. (*v*) [O III] λ5007, $\phi = 30°$, $T = 3 \times 10^4$ K.

If the slit is narrower than the HH object the predicted line profiles alter radically. The ratio of slit/HH size was taken to be 0.4 for the profile in Figure 3*t*. A narrow slit removes a large fraction of the emission from the wings of the bow (radial velocities between -40 and 10 km s^{-1}. The fully preionized model in Figure 3*u* emphasizes the low velocity shocks more (see also Tables 1 and 2). Finally, Figure 3*v* shows that the high-excitation line [O III] λ5007 can differ significantly from Hα, since [O III] λ5007 forms only in regions where $V_\perp$ is large.

c) Theoretical Line Ratios

Table 3 lists line ratios for various bow shocks. Results show a mixture of high-excitation and low-excitation lines, as expected from an object containing a variety of shock velocities. The high-excitation line [O III] λ5007 only appears when $V_s > 100$ km s^{-1} (Table 1). Table 3 shows that the bow shape also influences this line, however; more blunt shapes (like DA) have stronger O III emission. The strength of the [O II] λ3726/3729 lines would be a reliable measure of the preshock number density (the lines are sensitive to collisional deexcitation) were it not for the effect of the preionization state. The [O II] lines are much stronger when the incident gas is fully preionized. As discussed in § III*b*, the low-excitation optical forbidden lines ([O I], [S II], [N II]) generally increase in strength relative to Hβ as shock velocity increases until collisional deexcitation becomes important.

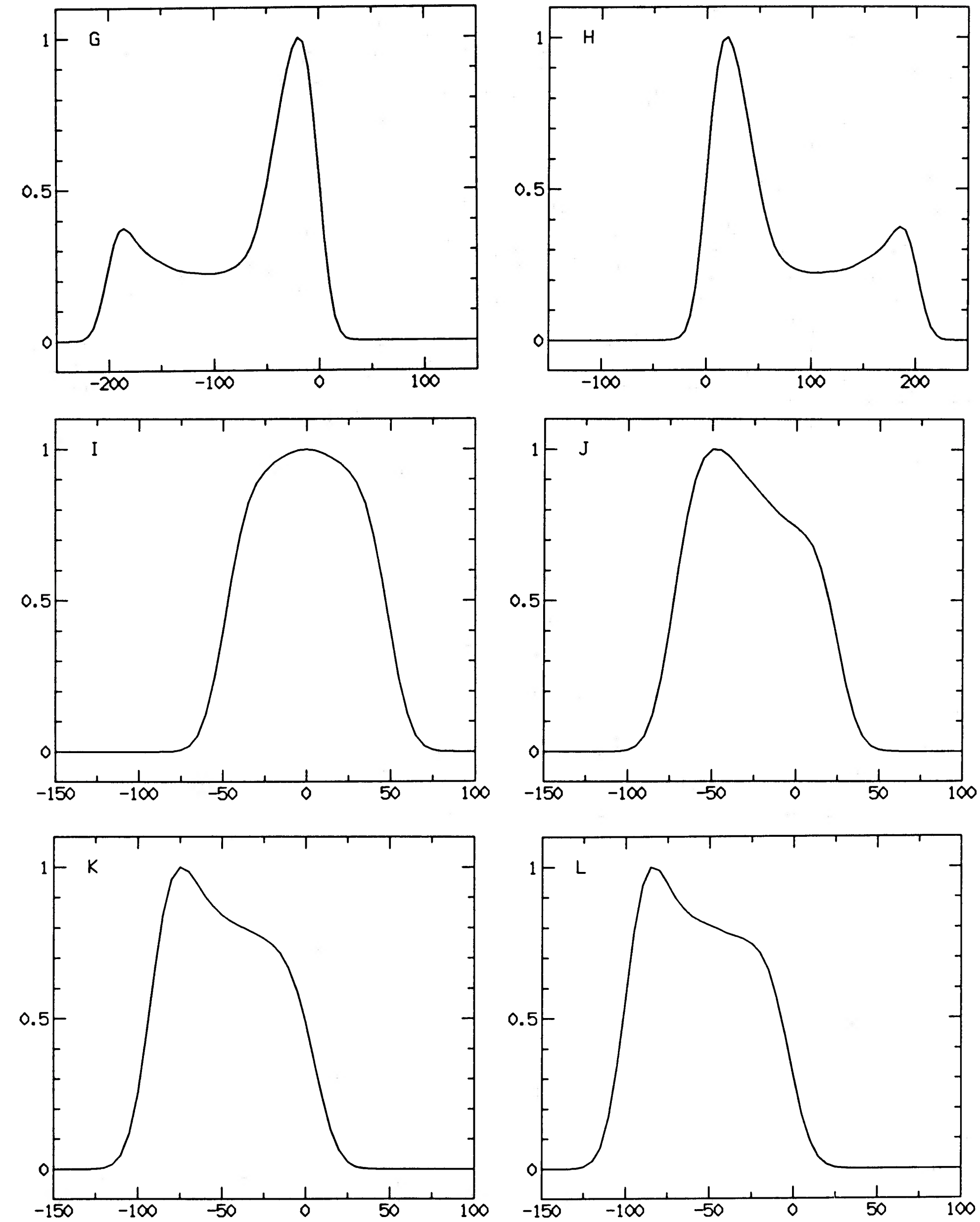

FIG. 3.—*Continued*

V. APPLICATION OF THE BOW SHOCK MODEL TO REGIONS CONTAINING HH OBJECTS

a) *The HH 1/2 Region*

The group of HH objects comprising HH 1 and 2 in some ways constitute an ideal laboratory for testing bow shock models of HH objects. There are a dozen or so HH objects in this region, all intrinsically bright, making high-resolution optical observations and UV flux measurements feasible. In fact, HH 2H is the only object for which reliable reddening corrected fluxes exist in the ultraviolet, and hence is the only object that can be compared directly against the predicted line ratios from the bowshock models. Since HH 1 and 2 lie on opposite sides of the exciting source (Pravdo *et al.* 1985; Strom *et al.* 1985) and the HH objects show large proper motions away from the exciting source (Herbig and Jones 1981), the flow must be oriented nearly in the plane of the sky. The source velocity is also known ($+9$ km s^{-1} $V_{\rm lsr}$; Torrelles *et al.* 1985*a*). This information is needed for the line profile analysis since radial velocities must be referenced to the source velocity.

Some facets of HH 1 and 2 complicate study of this outflow, however. Herbig and Jones (1981) have shown the morphology of HH 1 to vary substantially on time scales of decades. Since the emission from HH 1 is clumpy, a single aperture probably includes emission from more than one clump, each of which could represent a radiating bow shock. The situation for HH 2 is less severe, since the HH objects are more distinct for that group. Extended background emission also complicates

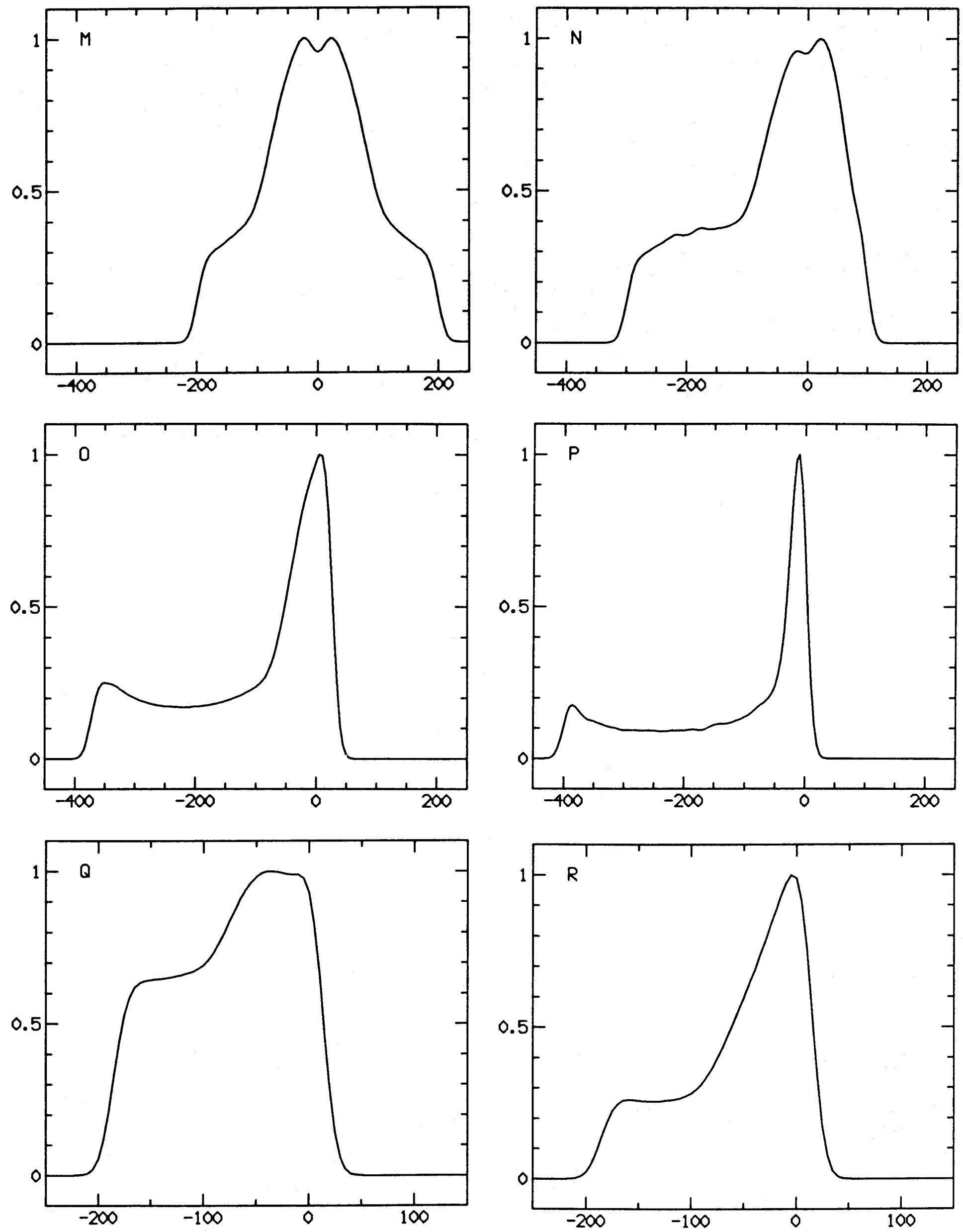

FIG. 3.—*Continued*

analysis of HH 1 and 2 (Böhm and Solf 1985; Strom *et al.* 1985). Such emission alters the observed line profiles, and also affects estimates of V_s and ϕ (§ IV*a*) since background emission will make any extended line wings appear less significant.

Several high-resolution studies of HH 1 and 2 exist in the literature (Schwartz 1981; Hartmann and Raymond 1984; Böhm and Solf 1985). For each HH object the observed profiles are centered near zero radial velocity and are roughly symmetrical, precisely the behavior predicted by the bow shock models for $\phi \sim 90°$. Figure 4 presents a number of line profiles of HH 1 and 2 taken with the facility echelle on the MMT. This instrument has a resolution of 12 km s^{-1} as determined from the FWHM of the calibration ThAr lines, and an effective aperture of 1".5 × 2".5 on the sky. Positions for the objects can be found in Herbig and Jones (1981).

We begin the analysis by extracting MX and MN from each observed profile and computing V_s and ϕ as prescribed in § IV*b*. Results appear in Table 4. In this table we also include spectra from Hartmann and Raymond (1984) for Hα and [N II] as well as some unpublished [O I] line profiles. The angle ϕ was measured assuming the bullet model with a stationary ambient medium ($\gamma = -V_s \cos \phi$ in eq. [10]).

The velocity widths for different lines within a given knot are quite similar, in agreement with the bow shock prediction. However, the strict equality of line widths predicted by equation (11) is not precisely obeyed. A clear trend is apparent, in the sense that the [O III] line widths are always larger than Hα and [N II]. The [S II] and [O I] widths are also generally slightly smaller than Hα, although the differences are small and may be affected by the lower signal-to-noise in spectra of these

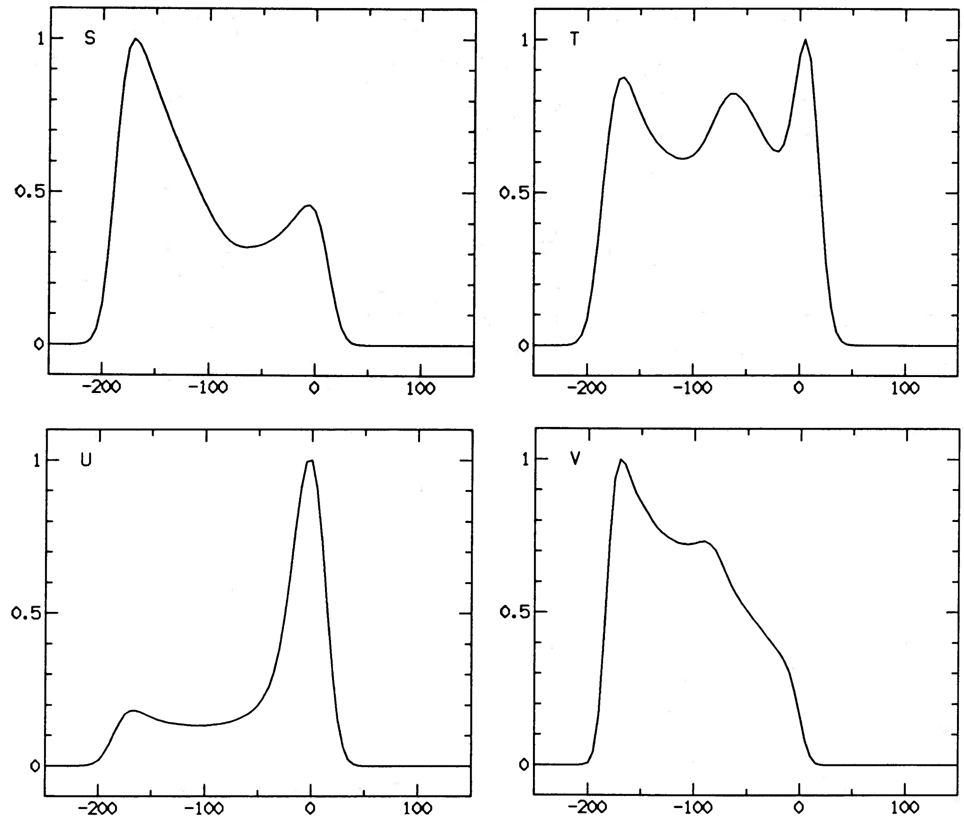

FIG. 3.—*Continued*

lines and possible contamination from narrow background emission components (Fig. 4*a*).

Differences in emission widths are direct indications of the failure of the assumption that the emission region can be approximated by a combination of individual planar shocks. Thermally unstable cooling of the highest velocity shocks might create substantial turbulent velocities, decaying rapidly enough to affect [O III] proportionately more than Hα. It is more likely that longer cooling times near the bow shock's apex make it possible for some of the velocity of this gas to be deflected normal to the bow shock axis while the gas is still hot (and emitting [O III]).

The two knots that have the largest discrepancy between [O III] and Hα widths, HH 1F and HH 2A′, may reflect additional complexities. HH 1 is composed of several different knots quite close together spatially (Herbig and Jones 1981), so that a single aperture might include emission from portions of several bow shocks. The line profile for HH 2A′ is strongly asymmetric (Fig. 4; also Hartmann and Raymond 1984), and Herbig and Jones (1981) suggested that this knot has appeared relatively recently, so perhaps time-dependent effects as well as lack of symmetry may have something to do with departures from the simple bow shock model. Choe, Böhm, and Solf (1985) claimed HH 1 was a single bow shock. However, in this case the observing slits would easily resolve the object, and the line profiles would be strongly double-peaked. The present data, as well as the line profiles presented by Böhm and Solf (1985) and Hartmann and Raymond (1984) for other positions in HH 1 (1A, 1C, 1D), provide no evidence for double peaks. Choe, Böhm, and Solf (1985) were forced to adopt very large turbulent velocities to avoid this problem. We feel it is much simpler to assume that the bow shocks present must be no more than 3″–4″ in size.

Orientation angles predicted from the various lines remain remarkably constant within each knot. *MX* and *MN* are sensitive to small changes in ϕ for $\phi \sim 90°$ (§ IV*b*), so the orientation angles are easy to estimate accurately for HH 1 and 2. Centroid radial velocities for nine of the 12 knots observed in HH 1 and 2 are negative, with HH 2M, 2E, and 2C the only exceptions (Table 4). The 45° dispersion of orientation angles within HH 2 is peculiar, but it is undeniably real. Since the objects only subtend $\sim 20°$ as seen from the source, the flow's opening angle apparently increases with distance. The objects comprising HH 2 seem to outline a cone of opening angle $\sim 50°$ (see Herbig and Jones 1981; or Strom *et al.* 1985), and perhaps the objects move within this cone. The wide opening angle can be taken to suggest either that a bullet has broken up, perhaps by the Rayleigh-Taylor instability shown in the plots of Różyczka and Tenorio-Tagle (1985*b*), or that the flow resembles the focused wind predicted by Cantó and Rodríguez (1980).

Using $\phi = 75°$ and $V_s = 160$ km s^{-1} (Table 4) we can generate theoretical line profiles for HH 2H. These are shown in Figures 4*e* and 4*f* for Hα and [O III] λ5007 along with observed profiles. We used a 160 km s^{-1} bow shock with equilibrium preionization, shape A, preshock density 500 cm^{-3}, bullet geometry, $\phi = 75°$, slit wider than the HH object, 12 km s^{-1} instrumental broadening, $T = 10^4$ K for Hα, and $T = 3 \times 10^4$ K for [O III] λ5007. The overall agreement is good, although the model profiles are somewhat too boxy in shape. These

TABLE 3

PREDICTED LINE RATIOS FROM THE BOW SHOCK MODEL

Model	1	2	3	4	5	6	7	8	9	10	11	12	13	Model[2]	Obs[2]
Shape	DA	RAGA	A	A	A	A	A	A	A	A	A	A	A	A	
Velocity (km/s)	200	200	200	100	200	200	30	50	100	150	200	300	400	160	
Preionization	Eq	Eq	Ion	Ion	Eq	Eq	Eq	Eq	Eq	Eq	Eq	Eq	Eq	Eq	
η (cm^{-3})	300	300	300	300	1000	100	300	300	300	300	300	300	300	500	
Hβ Flux[1]	86	77	41	10	272	27	0.24	2.2	22	44	82	191	340	85	309
He II 304	2452	1687	545	403	1737	1741	0	0	157	2270	1732	1457	1446	2204	
C III 977	813	581	753	940	630	615	0	1	217	711	616	547	506	672	
N III 991	110	76	92	74	86	84	0	0	17	80	84	79	74	86	
O VI 1035	1325	918	1105	0	1415	1417	0	0	0	38	1410	2773	2638	98	
Ne V] 1141	34	23	27	0	34	34	0	0	0	4	34	53	53	8	
S III 1198	123	87	108	101	98	96	0	1	32	92	96	91	86	94	
Si III 1206	153	114	208	286	127	122	0	0	95	116	122	113	104	120	
Lyα 1216	4910	6020	3766	3790	5837	5689	15533	9632	6867	6098	5741	5493	5523	6022	
O V] 1218	241	160	178	1	213	214	0	0	0	46	213	227	221	90	
N V 1240	244	161	177	1	209	211	0	0	0	62	209	234	224	122	
C II 1336	216	164	264	336	172	172	45	20	106	186	171	151	139	182	46;108
Si IV 1397	64	47	59	76	50	50	0	0	30	52	50	46	42	51	49;168
O IV] 1402	209	139	153	26	170	170	0	0	0	93	169	173	170	124	
N IV] 1486	44	29	34	11	30	35	0	0	1	28	33	33	32	31	
C IV 1549	882	596	654	317	665	665	0	0	15	711	662	599	563	699	385;521
[Ne V] 1574	3	2	2	0	3	3	0	0	0	0	3	4	4	1	
[Ne IV] 1601	19	12	13	2	18	15	0	0	0	8	16	19	19	11	
He II 1640	48	32	50	53	37	36	0	0	1	36	36	43	54	37	26;66
O III] 1663	155	106	123	85	123	122	0	0	21	97	122	119	115	109	74;255
N III] 1750	48	33	39	33	37	37	0	0	9	35	37	35	33	37	38;59
Si III] 1891	149	111	200	257	126	118	0	0	90	114	119	112	105	118	-;76
C III] 1908	327	237	285	348	264	249	1	3	112	278	252	231	219	269	163;392
N II] 2141	14	11	16	18	12	11	2	2	7	11	11	11	11	12	
C II] 2326	209	174	248	293	199	177	242	84	118	183	181	192	204	185	308;854
Si II] 2340	9	9	9	10	12	9	31	11	8	9	10	13	17	9	
[Ne IV] 2423	89	60	66	12	65	77	0	0	0	41	74	82	80	49	
[O II] 2470	54	40	47	43	62	39	1	2	23	38	44	47	48	45	
Mg II 2799	174	167	216	215	282	156	636	165	90	135	184	351	506	164	
Mg I 2852	31	24	20	9	35	26	38	10	5	19	28	55	59	23	
[O II] 3726	199	159	358	424	58	196	17	31	130	169	164	142	128	140	211;222
[O II] 3729	102	85	280	361	22	104	23	27	80	93	85	71	63	73	
[Ne III] 3869	49	35	38	32	40	39	0	0	13	33	39	46	56	35	16;15
Ca II 3945	124	99	80	37	166	102	186	51	27	74	116	225	254	94	16;48

TABLE 3—*Continued*

Model	1	2	3	4	5	6	7	8	9	10	11	12	13	Model[2]	Obs[2]
[Ne III] 3968	16	11	12	10	13	12	0	0	4	11	12	15	18	11	6;5
[S II] 4072	78	59	48	26	108	58	44	18	19	48	69	120	137	62	73;70
Ca I 4227	12	9	8	3	12	10	9	3	2	8	11	17	14	9	
[O III] 4363	24	17	19	14	19	19	0	0	4	16	19	19	18	17	13;15
[Fe III] 4658	8	6	12	15	7	6	0	0	5	6	7	6	6	7	8;-
Hβ 4861	100	100	100	100	100	100	100	100	100	100	100	100	100	100	100;100
[O III] 4959	91	63	70	53	70	71	0	0	15	61	71	70	70	66	27;29
[O III] 5007	264	183	203	154	203	208	0	0	43	178	206	204	203	191	83;81
[N I] 5200	19	28	21	18	18	30	228	61	20	27	27	36	31	25	9;11
[N II] 5755	5	4	5	5	5	4	1	1	2	4	4	5	6	4	5;7
He I 5876	13	9	16	16	10	11	0	0	3	10	11	15	16	10	7;7
[O I] 6300	160	146	83	28	204	150	471	159	60	125	162	298	329	142	113;138
[O I] 6363	53	49	28	9	68	50	157	53	20	42	54	99	110	47	36;50
[N II] 6548	47	38	51	45	30	45	19	19	22	36	42	48	51	35	-;47
Hα 6563	301	317	304	308	312	314	485	379	318	317	314	310	310	316	283;343
[N II] 6583	139	113	149	133	87	133	58	55	66	105	122	142	151	103	133;182
[S II] 6716	40	50	59	60	30	55	334	91	35	49	50	61	52	44	38;43
[S II] 6731	73	69	82	72	43	81	246	77	38	67	73	98	85	61	67;85
[Ar III] 7136	13	9	12	11	11	10	0	0	4	10	10	11	11	10	2;-
[Ca II] 7307	34	27	21	9	42	28	41	13	7	21	31	56	57	26	-;28
[O II] 7320	40	29	35	32	46	29	0	1	17	28	32	34	36	33	67;96
[O II] 7331	32	24	28	26	36	23	0	1	14	23	26	28	29	27	
[Fe II] 8617	11	12	7	4	16	11	76	18	7	10	12	20	24	11	
[C I] 8727	19	13	10	4	27	13	4	3	3	11	16	37	46	14	
[S III] 9069	12	11	8	6	11	12	9	9	6	11	11	20	26	11	
[S III] 9532	32	28	19	15	29	30	24	24	17	28	30	52	67	27	-;9
[C I] 9823	86	67	68	38	52	85	47	33	23	59	77	135	110	57	-;4
[C I] 9850	255	198	201	113	155	250	140	98	66	173	228	400	326	170	-;8
[S II] 10314	28	21	17	9	38	20	15	6	7	17	24	42	48	22	-;11
[S II] 10348	25	19	15	8	35	18	14	6	6	16	22	38	44	20	
[N I] 10402	8	6	5	2	12	6	8	3	2	5	7	16	21	7	-;12
He I 10830	20	16	18	17	16	17	1	1	13	17	16	22	24	16	-;105
[Ne II] 12.8μ	128	110	80	50	119	121	194	101	49	102	121	171	155	105	
[Ne III] 15.6μ	36	26	28	20	20	33	1	1	9	24	30	76	90	22	
[Fe II] 26.0μ	240	241	197	136	211	265	934	324	134	224	254	361	340	222	
[Si II] 35.3μ	132	362	219	270	244	331	4179	1154	360	374	317	277	247	330	
[O I] 63.2μ	148	168	109	71	179	175	955	270	100	148	177	176	143	150	
2 photon	1690	2194	1314	1336	2110	2061	7235	3956	2435	2212	2081	1994	2067	2180	-;12900

[1] The Hβ flux in units of 10^{-15} ergs cm^{-2} s^{-1} seen at Earth from the entire radiating bow shock at a distance of 500 pc using $R_0 = 1.5 \times 10^{16}$ cm for shape A, 8.1×10^{15} cm for the Raga shape, and 5.6×10^{15} cm for shape DA. These choices for R_0 lead to angular diameters ~4″ for the HH objects.

[2] Two independent sets of dereddened fluxes are given for HH 2H for both the ultraviolet and visible lines. The UV data come from Böhm-Vitense *et al.* (1982) and Brugel, Shull, and Seab (1982). The optical data is taken from Brugel, Böhm, and Mannery (1981) and Dopita, Binette, and Schwarz (1982). IIDS fluxes are used from Brugel, Böhm, and Mannery (1981) except for $\lambda > 7200$ Å, where only MCSP observations are available. The disagreements between the two sets of ultraviolet data arise primarily from the different reddening corrections applied. The value of 67 listed for [O II] 7320 refers to the sum of [C II] 7307 + [O II] 7320 + [O II] 7331, and the value of 96 listed for [O II] 7320 refers to the sum of [O II] 7320 and [O II] 7331. The values of 49 and 168 listed for Si IV 1397 refer to the total flux from the lines near 1400 Å, and the observed values for [O II] 3726 include the flux from [O II] 3729 also.

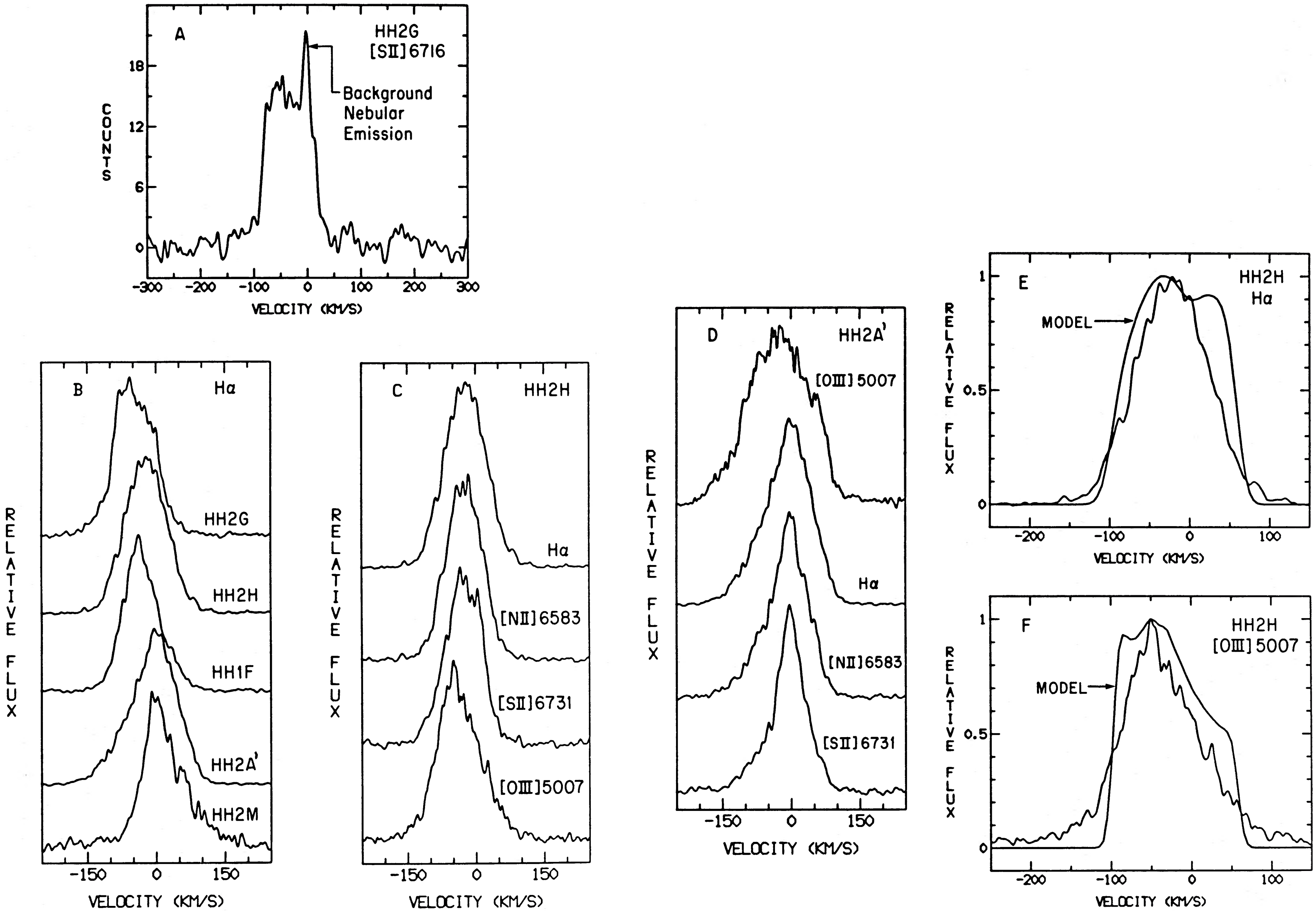

FIG. 4.—Line profiles and models for HH 1 and 2. The line profiles were taken 1984 November 10 with the facility echelle on the MMT (12 km s^{-1} resolution). Profiles are plotted vs. radial velocity with respect to the exciting source. The 160 km s^{-1} models used in (*e*) and (*f*) are described in the text.

TABLE 4

RESULTS

Object	Line	[1]MX(km/s)	[1]MN(km/s)	[2]Vs (km/s)	[2]Φ	[3]V_1(km/s)
HH 1A	Hα	20	-49	69	65°	63
	[N II] 6583	30	-49	79	76°	77
	[O I] 6300	25	-58	83	67°	76
HH 1C	Hα	46	-89	135	71°	128
	[N II] 6583	51	-86	137	75°	132
	[O I] 6300	26	-52	78	71°	74
HH 1D	Hα	39	-98	137	64°	123
	[N II] 6583	33	-95	128	61°	112
	[O I] 6300	48	-82	130	75°	126
HH 1F	Hα	42	-106	148	65°	134
	Hα	49	-99	148	70°	139
	[N II] 6583	41	-100	141	61°	128
	[N II] 6583	43	-88	131	70°	123
	[O I] 6300	31	-95	126	59°	108
	[O III] 5007	81	-131	212	76°	206
	[S II] 6716	23	-82	105	56°	87
	[S II] 6731	26	-83	109	59°	93
HH 2A'	Hα	98	-109	207	87°	206
	Hα	82	-124	206	78°	201
	[N II] 6583	90	-100	190	87°	189
	[N II] 6583	74	-122	196	76°	190
	[O I] 6300	77	-82	159	88°	159
	[O III] 5007	94	-172	266	73°	254
	[S II] 6716	68	-90	158	82°	156
	[S II] 6731	69	-101	170	79°	167
HH 2B	Hα	52	-81	133	77°	130
	[N II] 6583	47	-95	142	70°	133
HH 2C	Hα	62	-52	114	95°	114
	[N II] 6563	60	-45	105	98°	104
HH 2D	Hα	41	-79	120	72°	114
	[N II] 6563	19	-83	102	51°	79
	[O I] 6300	20	-61	81	60°	70
HH 2E	Hα	40	-32	72	96°	72
	[N II] 6583	41	-25	66	104°	64
	[O I] 6300	37	-20	57	107°	55
HH 2G	Hα	38	-118	156	59°	134
	Hα	28	-125	153	51°	119
	[N II] 6583	32	-116	148	55°	121
	[N II] 6583	17	-123	140	41°	92
	[O I] 6300	29	-115	144	53°	115
	[S II] 6716	29	-98	127	57°	107
	[S II] 6731	23	-118	141	48°	105
HH 2H	H α	60	-102	162	75°	157
	Hα	53	-105	158	71°	149
	[N II] 6583	49	-110	159	67°	146
	[N II] 6583	53	-105	158	71°	149
	[O I] 6300	49	-91	140	73°	134
	[O III] 5007	63	-128	191	70°	180
	[S II] 6716	36	-121	157	57°	132
	[S II] 6731	46	-115	161	65°	146
HH 2M	Hα	123	-61	184	110°	173
	[N II] 6583	112	-63	175	106°	168
	[S II] 6731	119	-48	167	115°	151
HH 7	Hα	-4	-112	108	-	-
HH 8	Hα	-7	-133	126	-	-
HH 10B	Hα	-20	-96	76	-	-
HH 11	Hα	-124	-246	122	-	-

TABLE 4—*Continued*

Object	Line	[1]MX(km/s)	[1]MN(km/s)	[2]V_s(km/s)	[2]Φ	[3]V_1(km/s)
HH 32A	Hα	353	0	353	149°	182
	[N II] 6583	356	11	345	157°	135
	[O III] 5007	380	10	370	157°	145
	[S II] 6716	333:	8	325:	154°:	142:
	[S II] 6731	351:	8	343:	154°:	150:
HH 32B	Hα	393	-21	414	141°	261
	[N II] 6583	400	-13	413	145°	237
	[S II] 6716	405	-6	411	148°	218
	[S II] 6731	408	-11	419	146°	234
HH 32C	Hα	12:	-344:	356:	32°:	189:
HH 32D	Hα	379	0:	379:	0°:	0
Cep A-A	Hα	12	-107	119	37°	72
	[N II] 6583	6	-105	111	27°	50
Cep A-B	Hα	4	-170	174	17°	51
	[N II] 6583	26	-169	195	43°	133
Cep A-C	Hα	10	-197	207	25°	87
Cep A-D	Hα	25	-214	239	38°	147
Cep A-E	Hα	16	-376	392	23°	153
Cep A-F	Hα	25	-96	121	54°	98
	[N II] 6583	7	-72	79	35°	45
Cep A–G[4]	Hα	57:	-77:	134:	81°	132:
Cep A-H	Hα	54	-326	380	44°	264
Cep A-HW	Hα	16	-460	476	21°	171
Cep A-S	Hα	39	-317	356	39°	224
	[N II] 6583	35	-318	353	37°	212

[1] Values of MX and MN were extracted from the high-resolution spectra according to the procedure described in § IV*b*. Values of SM used were 26 km s^{-1}, 14 km s^{-1}, 18 km s^{-1}, and 12 km s^{-1}, respectively, for the lines of H, N II, O III, and S II. Multiple listings for some lines were obtained from separate spectra and are included to show the degree of consistency among different measurements.

[2] The shock velocity was found from eq. (11). The orientation angle given is that of a bullet ramming into a stationary medium for HH 1/2 and Cep A; the medium is taken to move 25 km s^{-1} radially for HH 32A, B, and C. HH 32D assumed to be a stationary cloudlet for calculation of Φ.

[3] Predicted proper motion for the values of V_s and Φ in the table ($V_1 = V_s \sin \Phi$).

[4] A spike in the line profile of this object confuses the calculation of MX and MN, but the line profile is definitely centered near zero radial velocity.

same model parameters can be used to predict the emission-line fluxes expected from HH 2H. Results appear in Table 3 along with two sets of observed optical and UV line ratios corrected for reddening. The predicted bow shock fluxes generally agree for most of the bright lines throughout both the ultraviolet (Böhm-Vitense *et al.* 1982; Brugel, Shull, and Seab 1982) and visible (Brugel, Böhm, and Mannery 1981; Dopita, Binette, and Schwartz 1982) portions of the spectrum. Exceptions include [O III] λ5007/4959 and Ca II λ3945 (predicted to be about twice as bright as observed), and [C I] λ9850/9823, which is greatly overestimated in the models. The lack of prominent [C I] lines in HH 2H may reflect the lack of molecular cooling in the models. Some disagreement also appears between the observed and predicted two photon continuum fluxes, but this discrepancy is not serious since the observations are difficult to obtain accurately, and the model fluxes vary if the bow shape is altered. Emission from a cloudlet shock could also enhance the two photon flux.

The agreement between observed and predicted line ratios is the best to date for any shock model of HH objects. Choosing a normalization $R_0 = 1.5 \times 10^{16}$ cm to fix the size of HH 2H at 4″ (D = 500 pc) we predict the absolute Hβ flux to be 8.5×10^{-14} ergs cm^{-2} s^{-1} at Earth. Brugel, Böhm, and Mannery report 3.1×10^{-13} ergs cm^{-2} s^{-1} for HH 2H. The discrepancy can be reduced if the preshock density (500 cm^{-3}) is increased, since the Hβ flux scales linearly with density. If the preshock density is chosen too large, however, the [O II] λ3726/3729 lines will suffer enhanced collisional deexcitation and will become unacceptably weak compared with observed values (Tables 1 and 3; § IV*c*). A more accurate bow shock model including correct preionization should raise the [O II]/Hβ ratio (§ III*a*), so that a larger preshock number density can be used to increase the predicted Hβ flux. The Hβ flux of HH 2H is 2.7 times intrinsically brighter than that of HH 32A (which has a shock velocity ≈ 400 km s^{-1}), and 62 times brighter than HH 11 (distances from Herbig and Jones 1983;

fluxes from Brugel, Böhm, and Mannery 1981), so the large luminosities of HH 1 and 2 may be peculiar to the region.

Since a single bow shock model reproduces the observed line profiles and ratios quite well, the model must be generally correct. The observations of HH 1 and 2 provide direct evidence favoring a bullet model for HH objects. Proper motions of HH objects ejected in the plane of the sky must equal the shock velocities for the bullet model. The predicted proper motions (Table 4) are roughly the same as the observed values, although there is some tendency for the observed motions to exceed the predicted values. The approximate equality of predicted and observed proper motions favors the bullet model, since in the cloudlet model any such agreement would be coincidental. The physical parameters derived for HH 1 and 2 are in general agreement with earlier studies, but more precise. Hartmann and Raymond (1984) did not consider their models accurate enough for a detailed fit to observed line intensities, but their 160 and 200 km s^{-1} bow shock models resembled the observed line strengths and widths more closely than a 300 km s^{-1} model. A recent study of the line fluxes in HH 2 by Cantó and Rodríguez (1986) reveals a correlation between Hα fluxes and the square of the total velocity, consistent with the present bow shock and planar shock models (Tables 1, 2, and 3). This correlation provides additional support for the bullet model. The analyses of Choe, Böhm, and Solf (1985), Raga and Böhm (1985), Böhm and Solf (1985), and Hartmann and Raymond (1984) favored the bullet model over the shocked cloudlet model, in agreement with the present results.

b) HH 32/AS 353A

The T Tauri star AS 353A and its associated HH objects present a difficult challenge for any model of HH emission. Four HH objects are present; HH 32A, B, and D are redshifted and located west of AS 353A, while HH 32C is blueshifted and situated east of the star (Mundt, Stocke, and Stockman 1983). Each HH object possesses line widths exceeding 350 km s^{-1}, with double-peaked profiles evident for most of the low-excitation lines (Hartigan, Mundt, and Stocke 1986; Solf, Böhm, and Raga 1986). Hα line profiles of HH 32A and B differ markedly from that of D. In addition, the [O III] λ5007 and Hα line profiles differ in HH 32A, with [O III] λ5007 showing only a single peak. The number density in the two-velocity peaks appears identical for each HH object. The system also has a redshifted linear jet (Hartigan, Mundt, and Stocke 1986).

Since extinction apparently increases dramatically from west to east across the source, reliable dereddened line ratios are difficult to obtain, but the presence of C IV λ1549 indicates large shock velocities (Böhm and Böhm-Vitense 1984; Brugel, Böhm, and Mannery 1981). Although proper motions of HH 32A and B are directed away from AS 353A, the inferred velocities are quite different (54 and 202 km s^{-1}, respectively), but the uncertainties in these values are also large ($\pm 3\ \sigma$) uncertainties are 45 km s^{-1}; Herbig and Jones 1983). AS 353A is located about 300 pc from the sun (Herbig and Jones 1983), has a $V_{\rm lsr}$ velocity of +8 km s^{-1} (Edwards and Snell 1982), and a luminosity 6.6 $L_\odot$ (Cohen *et al.* 1984).

Despite widely varying line profiles for the different emission lines of HH 32A, B, C, and D, the lines have the same FWZI for a given object (see Fig. 7 of Hartigan, Mundt, and Stocke 1986, and also Table 4 of this work), as predicted by the bow shock models. The inferred shock velocities for HH 32A, B, C, and D are (Table 4) 360, 415, 360, and 380 km s^{-1}, respectively. These shock velocities are close to the terminal wind velocity of AS 353A (Hartigan, Mundt, and Stocke 1986). Line profiles for all four HH objects diminish rapidly near zero radial velocity, implying an oblique angle for the flow (135° $< \phi <$ 180°). We were able to match the HH 32A line profiles best with a bullet plowing into a medium moving +25 km s^{-1} radially, and with an orientation angle 150°. Model and observed line profiles for HH 32A are presented together in Figures 5*a*–5*e*. The large shock velocity and oblique viewing angle for HH 32A cause the double-peaked model line profiles (§ IV*b*). The models fit the data reasonably well, with double-peaked profiles predicted for Hα, [N II] λ6583, and the red [S II] doublet. The [O III] λ5007 line is observed to have a single broad peak, and the models also predict a more symmetrical profile for this line.

The models predict the high radial velocity peak to occur at somewhat larger velocities than is observed. The discrepancy could result due to the assumption of small cooling distances in the model (see § III*c*). This assumption becomes more suspect at large shock velocities. The cooling distance behind a 360 km s^{-1} shock with preshock density 1000 cm^{-3} is 475 AU from equation (8). This distance corresponds to 1"6 at 300 pc, approximately one-third the size of the HH objects. The first effect of a larger cooling distance for the bullet model will be to shift the apex emission to lower radial velocity, precisely the observed discrepancy in Figure 5. The models predict the [S II] λ6731/6716 ratio (which increases monotonically with density) to be somewhat larger for the high radial velocity peak than for the low radial velocity peak. The observed constancy of this ratio could also be a cooling distance effect, since the highest radial velocity gas (near the apex) should expand as the cooling distance grows, lowering the [S II] λ6731/λ6716 ratio for the high-velocity peak.

Since the low radial velocity peak outshines the high radial velocity peak for HH 32A, B, and C, these objects must be bullets. The peculiar HH 32D line profile agrees well with a stationary cloudlet model (Fig. 5*f*). If HH 32D is a cloudlet instead of a bullet, then the preshock density is that of the stellar wind, which is probably lower than the density of the ambient cloud (the preshock material in the bullet model). Hence, the cooling distance is larger for the cloudlet model, and we should observe a greater deviation from the model for HH 32D than HH 32A for the apex emission (which is near *zero* radial velocity for a stationary cloudlet). Figure 5*f* supports this hypothesis. HH 32D will also be fainter than the other knots (as observed) if its preshock density is lower.

From Table 4 we predict the following tangential motions for HH 32A, B, C, and D: 150 km s^{-1}, 240 km s^{-1}, 190 km s^{-1}, and 0 km s^{-1}. HH 32D should have no proper motion if it is indeed a shocked cloudlet as we suggest. The observed 202 km s^{-1} proper motion for object B agrees well with the predicted value, but matching the 54 km s^{-1} motion of HH 32A requires an orientation angle of 171° instead of 150° for V_s = 360 km s^{-1}. These flow parameters agree well with the position-velocity results of Solf, Böhm, and Raga (1986), and Raga and Böhm (1986) who found V_s = 300 km s^{-1} and ϕ = 160° for HH 32A. More precise proper motion measurements of HH 32A will clarify if a more oblique angle is indeed required for this object.

The ability of a single bow shock model to match the varied line profiles present in this region is strong evidence favoring the overall correctness of the model. How does the redshifted jet fit into this picture? A spectrum of the jet (Hartigan, Mundt, and Stocke 1986) revealed primarily Hα emission. It is not clear how much, if any, of the Hα in the jet is reflected from the

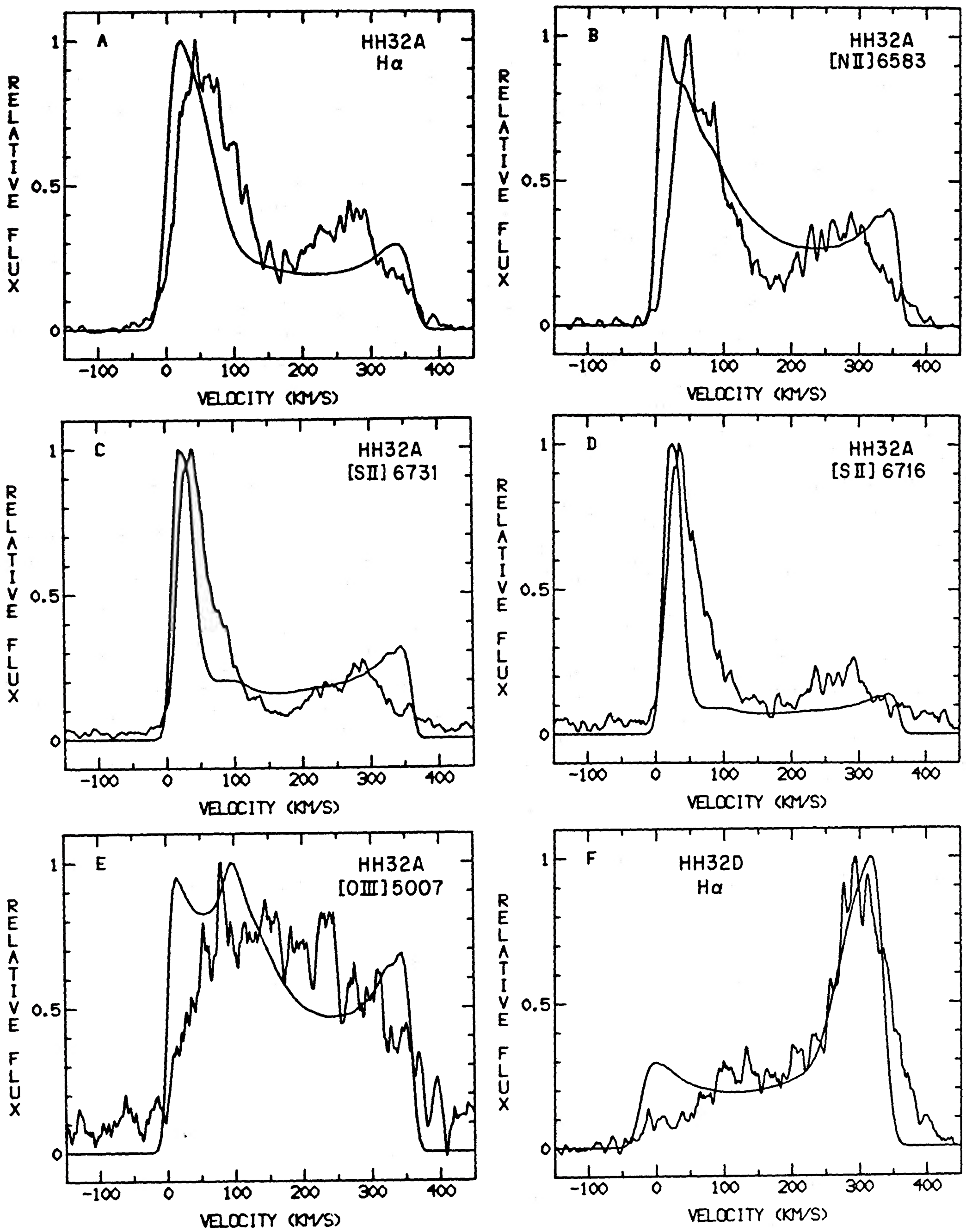

FIG. 5.—Model and observed line profiles for HH 32A and D. The observations were taken from Hartigan, Mundt, and Stocke (1986). For the HH 32A line profiles in (*a*)–(*e*), the model is a 360 km s^{-1} bow shock with equilibrium preionization, shape A, preshock density 1000 cm^{-3}, bullet geometry with a medium moving outward 25 km s^{-1} radially, $\phi = 150°$, slit wider than the HH object, 12 km s^{-1} instrumental broadening, $T = 30{,}000$ K for [O III], and $T = 10{,}000$ K for the other lines. (*f*) employs the same model for HH 32D, but with $\phi = 30°$ using a stationary cloudlet.

Hα emission line of AS 353A, but if the jet emission arises from shocks, then Tables 1 and 2 suggest low shock velocities with substantial preionization. Landau (1945) has shown that a weak shock must occur in the wake of a passing bullet, and the jet emission could arise from this shock. Alternatively, oblique shocks in a jet of material flowing outward in the bullet's wake would also contribute emission.

c) *Cepheus A*

A complex mixture of continuum peaks, masers, and molecular outflow characterizes the star formation region Cepheus A (see Hartigan and Lada 1985 for a review). Heavy obscuration conceals the luminous (2.5×10^4 $L_\odot$; Evans *et al.* 1981) source(s) driving the molecular outflow (Rodríguez, Ho, and Moran 1980). An area of nebulae 1ʹ.5 (0.3 pc for a 725 pc distance; Garmany 1973) west of the IR source contains 10 HH objects and two groups of reflection nebulae (Hartigan and Lada 1985). The HH objects are blueshifted even though they lie in the direction of the redshift molecular outflow (Lenzen, Hodapp, and Solf 1984), raising the possibility of differing driving sources for the CO outflow and HH emission. High-resolution Hα and [N II] spectra of the HH objects (Hartigan *et al.* 1986) reveal line profiles similar to HH 32; double-peaked profiles are evident in the spectra of knots E and S. The HH objects exhibit an extraordinary range of line widths, from nearly 500 km s^{-1} (the largest for any HH object) for knot HW, to a mere 100–140 km s^{-1} for knots A, F, and G. No flow orientation angle can be guessed *a priori* since no redshifted HH objects are seen, and no proper motions available. No line ratios have yet been measured for the HH objects either.

Values of MX and MN from the Hα profiles for each object are reproduced in Table 4 using $V_{\rm lsr} = -12$ km s^{-1} for Cepheus A (Torrelles *et al.* 1985*b*) and indicate a variety of shock velocities. The highest shock velocities (largest line widths) occur in objects HW (476 km s^{-1}), E (392 km s^{-1}), H (380 km s^{-1}), and S (355 km s^{-1}). These four knots are aligned roughly east-west and apparently define the flow's axis. The knots north of this axis, A, F, and G, have the smallest line widths (115 km s^{-1}, 100 km s^{-1}, and :134 km s^{-1}, respectively), while objects B, C, and D possess intermediate line widths.

The presence of double-peaked and highly asymmetrical line profiles for objects HW, E, H, and S demonstrates that HH 32A–D are not anomalous in this regard. Moreover, the maximum radial velocities seen in Cepheus A are near zero for each object except G. The emission from HH 32A–D also vanishes near zero radial velocity. The bow shock models show (§ IV*a*) that one extreme radial velocity should be near zero for an oblique flow. Such behavior is also apparent in the [O I] profiles of HH objects in M42 (Taylor *et al.* 1986), where one finds broad, asymmetrical line profiles that vanish near zero radial velocity and have a prominent low-velocity component. Double-peaked profiles occur for oblique ϕ only when $V_s >$ 150 km s^{-1}, as observed in Cepheus A. The inferred orientation angles (Table 4) lie between 20° and 45° for all objects except G. Although MX and MN are somewhat uncertain for G, the emission from this object is definitely centered near zero radial velocity, indicating motion nearly in the plane of the sky.

Objects S, H, HW, and E must be bullets since the strongest emission occurs in the low radial velocity peak. A bow shock model of object S is shown in Figure 6 together with a high-resolution Hα line profile from Hartigan *et al.* (1986). As for HH 32A, the position of the high radial velocity peak is not quite correct, perhaps due to the model's assumption of small cooling distances (§ V*b*), but the model does agree qualitatively with the data. The largest predicted proper motions are 264 km s^{-1} for H and 220 km s^{-1} for S. Object S outshines the other knots and might be bright enough to be seen in the UV, where high-excitation lines like C IV λ1549 should be visible. A comprehensive model for these objects awaits unambiguous identification of the exciting source and precise proper motion measurements of the HH objects.

d) HH 7–11

The B205 dark cloud lies 350 pc distant (Herbig and Jones 1983) and contains a variety of HH objects including a string of low-excitation knots labeled HH 7, 8, 9, 10A, 10B, and 11. The exciting star, SVS 13 (Strom, Vrba, and Strom 1976), has a luminosity of 66 $L_\odot$ (Cohen, Harvey, and Schwartz 1985) and drives a bipolar molecular outflow (Snell and Edwards 1981). The Herbig-Haro objects are located in the blueshifted part of the flow. A dense torus aligned perpendicular to the string of HH objects apparently collimates the outflow (Hodapp 1984). The gas surrounding SVS 13 is centered at +7.8 km s^{-1} $V_{\rm lsr}$. Only HH 11 exhibits detectable proper motion; this object moves away from SVS 13 at 58 km s^{-1} in the plane of the sky (Herbig and Jones 1983). Proper motion of HH 7 is more difficult to measure since this object is more extended than HH 11.

HH 7 and 11, along with HH 43, 34, and 47, make up a distinct class of low-excitation HH objects (see Böhm, Brugel, and Olmsted 1983; Böhm, Brugel, and Mannery 1980; Reipurth *et al.* 1986). These objects show [S II] λ4072 and [N I] λ5200 comparable to, or greater than, Hβ and have [S II]

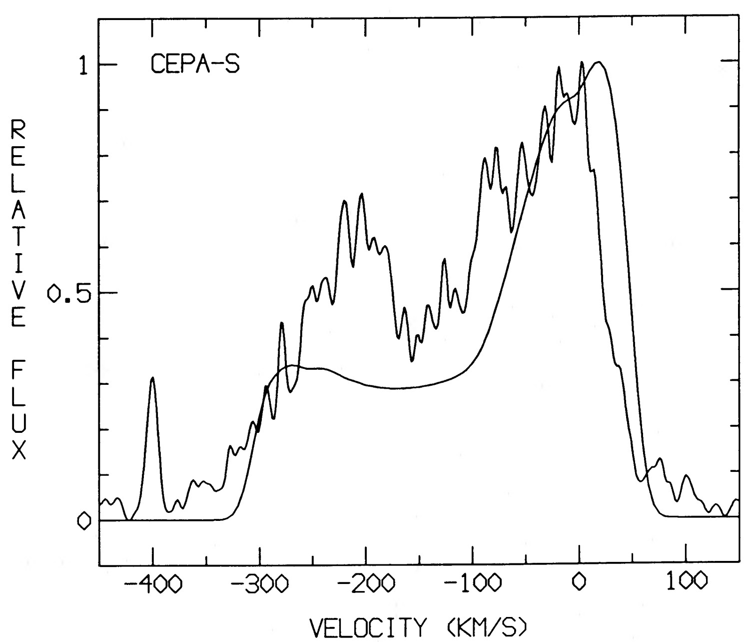

FIG. 6.—Hα line profile and bow shock model for object S in Cepheus A. The model is the same as the one displayed in Fig. 5, except here we employ bullet geometry with a stationary medium and $\phi = 45°$.

λ6716/6731 and [O I] λ6300/6363 fluxes exceeding Hα. In addition, no [O III] λ5007 emission is seen, the [N II] λ6583/6548 lines are weak, and [C I] λ9850/9823 can be as much as 6 times stronger than Hβ. The only lines present in the ultraviolet appear to be H_2, C II], [O II], and Mg II. A perusal of Table 1 reveals that these observed characteristics are all predicted accurately by the equilibrium planar shock models; specifically, the E20 and E30 models bracket the observations, with E30 fitting the data somewhat better (see also Table 3). The agreement between shock theory and observations indicates that emission from this peculiar class of low-excitation HH objects also arises from radiative shocks.

The low excitation spectra of HH 7 and 11 impose severe constraints on any bow shock model for these objects. Shock velocities of $\sim$30 km s^{-1} imply similar line widths for a bow shock. The line profiles of HH 7–11 in Figure 7 are indeed narrower than those of HH 1 and 2, but at 120 km s^{-1} (Table 4) they are still much too broad to arise from a 30 km s^{-1} bow shock. One way to explain the low-excitation spectra and the broad-line profiles in a single model would be to have a cloudlet shock be responsible for the bulk of the observed emission while the radiating bow shock contributes only to a broad underlying pedestal. It is also possible that a 100 km s^{-1} shock in molecular gas produces an emission-line spectrum resembling that of a much slower shock, since a substantial fraction of the postshock thermal energy is required to dissociate H_2 and additional thermal energy would be radiated away by the molecules.

The maximum radial velocity seen in the Hα profile of HH 11 is negative (Fig. 7). This cannot be explained with a bullet ramming into a stationary medium or with a stationary cloudlet, since both these models have positive maximum radial velocities with respect to the driving star (§ IV*a*). Assuming the FWZI to arise from bow shock emission, we examine the possibility of an accelerated cloudlet model for HH 11. The radial velocity of a moving cloudlet would have to exceed 110 km s^{-1} (blueshifted) to make HH 11 compatible with any cloudlet model. The 58 km s^{-1} tangential motion implies a space velocity exceeding 125 km s^{-1} for HH 11 with respect to SVS 13. Since the shock velocity for HH 11 is $\sim$120 km s^{-1}, the emerging stellar wind from SVS 13 must exceed 245 km s^{-1}. Unless a highly variable stellar wind is invoked, such a large wind velocity contradicts observations of HH 7, 8, and 10B (Fig. 7). These objects exhibit narrow ($\sim$100 km s^{-1}) line widths indicating low bow shock velocities, have low radial velocities, and show no detectable motion.

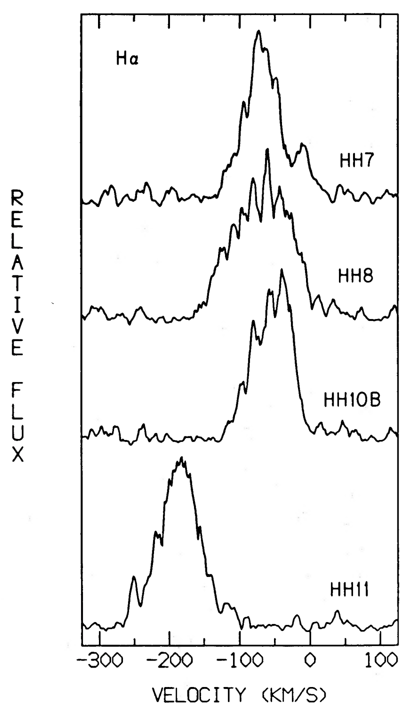

FIG. 7.—Hα line profiles of HH 7, 8, 10B, and 11 taken 1983 November 29 with the MMT echelle. The abscissa is radial velocity (km s^{-1}) with respect to SVS 13, the exciting star.

The velocities of HH 11 can also be explained by a bullet plowing into a medium which is already moving 110 km s^{-1} radially. With this picture, HH 7 would be the first ejected bullet; it, and subsequent bullets, would evacuate a cavity into which stellar wind material could flow, thereby providing a moving medium for the next bullet.

The line profile of HH 7 is consistent with a bullet plowing into a stationary medium, and although the equations from § IV*a* cannot be used to calculate an orientation angle due to the inferred contaminating cloudlet emission, the near-zero maximum radial velocity indicates that this object is angled considerably from the plane of the sky ($\phi \lesssim 45°$). Such an oblique angle implies that any proper motions observed should be small, as is observed.

In summary, the emission from Herbig-Haro objects 7 through 11 appears to arise mainly from 20–30 km s^{-1} shocks. The observed linewidths (100–120 km s^{-1}) are much too large for a 30 km s^{-1} bow shock, however. A model including both the cloudlet shock and bow shock emission may explain both the low-excitation spectra and the large line widths. Molecular cooling not included in our calculations might also help to eliminate the discrepancy. Assuming the FWZI of the emission lines to arise from a stationary cloudlet or from a bullet plowing into a stationary medium leads to a direct contradiction for the HH 11 line profile. The only acceptable picture for the HH 7–11 region is a bullet model where a stellar wind follows the initial bullets (HH 7, 8, 10), producing a moving medium for subsequent bullets.

VI. SUMMARY

We have investigated the kinematics, geometry, and physical parameters of radiating bow shocks as applied to HH objects. Three grids of radiative planar shock models completed clearly illustrate the dependence of the line fluxes on shock velocity, preshock density, and the preshock ionization state. The bow shock models incorporate the planar results into bow shock geometry and predict the line fluxes, ratios, and profiles expected from HH objects.

Results show that a mixture of high-excitation and low-excitation lines is expected from a bow shock. Any low-excitation line profile can be used to estimate the shock velocity and orientation angle of a bow shock. The shock velocity equals the FWZI for radiating bow shocks independent of orientation angle, preshock density, bow shock shape, and preshock ionization state. Orientation angles can be inferred from the position of maximum and minimum radial velocity assuming either a bullet or stationary cloudlet model provided the velocity of the exciting star is known. Inclusion of thermal and instrumental broadening alters the formulae for shock velocity and orientation angle only slightly. Double-peaked emission line profiles arise naturally from bow shocks for high (>150 km s^{-1}) shock velocities and oblique ($0° < \phi < 45°$, $135° < \phi < 180°$) orientation angles. Line profiles for the cloudlet model are simply reflections of bullet profiles about the centroid radial velocity. The centroid radial velocity of a line profile does not equal the radial velocity of the HH object, since the radiating gas moves with respect to the obstacle.

The bow shock model has been applied to four regions containing HH objects. From the line profiles of HH 1 and 2, we infer shock velocities on the order of the observed proper motions, suggesting that these objects are bullets. The orientation angles obtained from the profiles indicate ejection in the plane of the sky, consistent with the location of HH objects on both sides of the exciting star. Using the 160 km s^{-1} shock velocity deduced from the line profiles for HH 2H, the model reproduces the observed dereddened line ratios from the near-infrared to the ultraviolet for most lines. The HH objects in Cepheus A and HH 32 show very broad, and in many cases double-peaked, line profiles, indicative of large shock velocities and oblique orientation angles. The radial velocity peak near zero is stronger for each double-peaked object except HH 32D. Hence, only HH 32D agrees with the shocked cloudlet model, with the other objects apparently bullets.

Emission from the extremely low excitation objects HH 7–11 appears to arise from 20–30 km s^{-1} shocks. The much larger line widths of nearly 120 km s^{-1} pose a severe dilemma for any model. A combination of bow and cloudlet shocks can in principle account for the linewidths and line ratios. The best explanation for the observed radial velocities in HH 11 is a bullet shot into a moving medium.

Existing observations of HH objects such as line fluxes, line ratios, line asymmetries, double-peaked profiles, angular sizes, and proper motions provide numerous stringent constraints upon any model for HH emission. We have shown in this paper that a single unifying model—a radiating bow shock around a bullet—can explain most of the observations. The bullet model succeeds for objects with a wide range of shock velocities and orientations.

The bow shock models presented here could be improved with the inclusion of a cloudlet shock, molecular cooling, obstacle reddening, and more detailed preionization calculations. In addition, including a finite cooling distance in the calculations should modify the predicted line profiles somewhat when the shock velocity is large. It would be useful to develop a quantitative model for jet emission to see how this phenomenon relates to ejected bullets. Finally, more detailed investigation into the physics of bullet formation should be undertaken.

P. H. was funded by a NASA Graduate Research Fellowship during the course of this work. P. H. would like to thank C. Lada for his continuing support of the project and J. Stocke for assistance with the observations and useful comments on a preliminary draft of this paper. This research was supported in part by the Visitors Program of the Smithsonian Astrophysical Observatory.

REFERENCES

Binette, L., Dopita, M. A., and Touhy, I. R. 1985, *Ap. J.*, **297**, 476.
Böhm, K.-H., and Böhm-Vitense, E. 1984, *Ap. J.*, **277**, 216.
Böhm, K.-H., Brugel, E. W., and Mannery, E. 1980, *Ap. J. (Letters)*, **235**, L137.
Böhm, K.-H., Brugel, E. W., and Olmsted, E. 1983, *Astr. Ap.*, **125**, 23.
Böhm, K.-H., and Solf, J. 1985, *Ap. J.*, **294**, 533.
Böhm-Vitense, E., Böhm, K.-H., Cardelli, J. A., and Nemec, J. M. 1982, *Ap. J.*, **262**, 224.
Brugel, E. W., Böhm, K.-H., and Mannery, E. 1981, *Ap. J. Suppl.*, **47**, 117.
Brugel, E. W., Shull, J. M., and Seab, C. G. 1982, *Ap. J. (Letters)*, **262**, L35.
Cantó, J., and Rodríguez, L. F. 1980, *Ap. J.*, **239**, 982.
———. 1986, *Rev. Mexicana Astr. Ap.*, in press.
Choe, S.-U., Böhm, K.-H., and Solf, J. 1985, *Ap. J.*, **288**, 338.
Cohen, M., Harvey, P. M., and Schwartz, R. D. 1985, *Ap. J.*, **296**, 633.
Cohen, M., Harvey, P. M., Schwartz, R. D., and Wilking, B. A. 1984, *Ap. J.*, **278**, 671.
Cox, D. P. 1972, *Ap. J.*, **178**, 143.
Cox, D. P., and Raymond, J. C. 1985, *Ap. J.*, **298**, 651.
Cudworth, K. M., and Herbig, G. H. 1979, *A.J.*, **84**, 548.
DeYoung, D. S., and Axford, W. I. 1967, *Nature*, **216**, 129.
Dopita, M. A. 1978, *Ap. J. Suppl.*, **37**, 117.
Dopita, M. A., Binette, L., and Schwartz, R. D. 1982, *Ap. J.*, **261**, 183.
Edwards, S., and Snell, R. L. 1982, *Ap. J.*, **261**, 151.
Evans, N. J., II, *et al.* 1981, *Ap. J.*, **244**, 115.
Garmany, C. D. 1973, *A.J.*, **78**, 185.
Hartigan, P., and Lada, C. J. 1985, *Ap. J. Suppl.*, **59**, 383.
Hartigan, P., Lada, C. J., Stocke, J., and Tapia, S. 1986, *A.J.*, **92**, 1155.
Hartigan, P., Mundt, R., and Stocke, J. 1986, *A.J.*, **91**, 1357.
Hartmann, L., and Raymond, J. C. 1984, *Ap. J.*, **276**, 560.
Herbig, G. H., and Jones, B. F. 1981, *A.J.*, **86**, 1232.
———. 1983, *A.J.*, **88**, 1040.
Hodapp, K.-W. 1984, *Astr. Ap.*, **141**, 255.
Innes, D., Giddings, J. R., and Falle, S. A. E. G. 1986, in *Workshop on Model Nebulae*, ed. D. Péquinot (Paris: Observatoire de Paris), p. 153.
Landau, L. 1945, *J. Phys. U.S.S.R.*, **9**, 496.
Lenzen, R., Hodapp, K.-W., and Solf, J. 1984, *Astr. Ap.*, **137**, 202.
Luyten, W. J. 1971, *The Hyades* (Minneapolis: University of Minnesota Press).
McCray, R., Stein, R. F., and Kafatos, M. 1975, *Ap. J.*, **196**, 565.
Mundt, R., Stocke, J., and Stockman, H. S. 1983, *Ap. J. (Letters)*, **265**, L71.
Norman, C., and Silk, J. 1979, *Ap. J.*, **228**, 197.
Péquinot, D. 1986, in *Workshop on Model Nebulae*, ed. D. Péquinot (Paris: Observatoire de Paris), p. 363.
Pravdo, S. H., Rodríguez, L. F., Curiel, S., Cantó, J., Torrelles, J. M., Becker, R. H., and Sellgren, K. 1985, *Ap. J. (Letters)*, **293**, L35.
Raga, A. C. 1986, Ph.D. thesis, University of Washington.
Raga, A. C., and Böhm, K.-H. 1985, *Ap. J. Suppl.*, **58**, 201.
———. 1986, *Ap. J.*, **308**, 829.
Raymond, J. C. 1979, *Ap. J. Suppl.*, **39**, 1.
Raymond, J. C., Black, J. H., Dupree, A. K., Hartmann, L., and Wolff, R. S. 1981, *Ap. J.*, **246**, 100.
Reipurth, B., Bally, J., Graham, J. A., Lane, A. P., and Zealey, W. J. 1986, *Astr. Ap.*, **164**, 51.
Rodríguez, L. F., Ho, P. T. P., and Moran, J. M. 1980, *Ap. J. (Letters)*, **240**, L149.
Rózyczka, M., and Tenorio-Tagle, G. 1985*a*, *Astr. Ap.*, **147**, 220.
———. 1985*b*, *Acta Astr.* **35**, 213.
Sandford, M. T., II, and Whitaker, R. W. 1983, *M.N.R.A.S.*, **205**, 105.
Schwartz, R. D. 1978, *Ap. J.*, **223**, 884.
———. 1981, *Ap. J.*, **243**, 197.
———. 1983, *Ann. Rev. Astr. Ap.*, **21**, 209.
Schwartz, R. D., and Dopita, M. A. 1980, *Ap. J.*, **236**, 543.
Seab, C. G., and Shull, J. M. 1983, *Ap. J.*, **275**, 652.
Shull, J. M., and McKee, C. F. 1979, *Ap. J.*, **227**, 131.
Snell, R. L., and Edwards, S. 1981, *Ap. J.*, **251**, 103.
Solf, J., Böhm, K.-H., and Raga, A. C. 1986, *Ap. J.*, **305**, 795.
Spitzer, L. 1978, *Physical Processes in the Interstellar Medium* (New York: John Wiley and Sons).
Strom, S. E., Strom, K. M., Grasdalen, G. L., Sellgren, K., Wolff, S., Morgan, J., Stocke, J., and Mundt, R. 1985, *A.J.*, **90**, 2281.
Strom, S. E., Vrba, F. J., and Strom, K. M. 1976, *A.J.*, **81**, 314.
Taylor, K., Dyson, J. E., Axon, D. J., and Hughes, S. 1986, *M.N.R.A.S.*, **221**, 155.
Tenorio-Tagle, G., and Rózyczka, M. 1984, *Astr. Ap.*, **141**, 351.
Torrelles, J. M., Cantó, J., Rodríguez, L. F., Ho, P. T. P., and Moran, J. M. 1985*a*, *Ap. J. (Letters)*, **294**, L117.
Torrelles, J. M., Ho, P. T. P., Rodríguez, L. F., and Cantó, J. 1985*b*, *Ap. J.*, **288**, 595.

PATRICK HARTIGAN: Department of Planetary Sciences, University of Arizona, Tucson, AZ 85721

LEE HARTMANN and JOHN RAYMOND: Harvard-Smithsonian Center for Astrophysics, 60 Garden Street, Cambridge, MA 02138